VILLANOVA UNIVERSITY
College of Engineering

CAC
Center for Advanced Communications
College of Engineering, Villanova University

**FINAL TECHNICAL REPORT**

# Polarimetric and Indoor Imaging Fusion Based on Compressive Sensing

May 2011 – September 2012

**Submitted to**

**Office of Naval Research**

ONR Grant: N00014-11-1-0576


**Principal Investigator**

Moeness Amin

**Contributors**

Prof. Moeness Amin
Dr. Fauzia Ahmad
Dr. Jiang Qian
Ms. Eva Lagunas


**April 2013**

# Contents


**Executive Summary** ..... iii
**List of Publications** ..... vi
**Chapter 1 Through-the-Wall Human Motion Indication using Sparsity-Driven Change Detection** ..... 1
**1.1. Introduction** ..... 1
**1.2. Backprojection-based Change Detection** ..... 4
**1.3. Sparsity-Driven Change Detection under Translational Motion** ..... 7
**1.4. Sparsity-Driven Change Detection under Short Sudden Movement** ..... 11
**1.5. Experimental Results** ..... 15
**1.6. Conclusion** ..... 19
**1.7. References** ..... 20
**Chapter 2 Joint Localization of Stationary and Moving Targets behind Walls using Sparse Scene Recovery** ..... 30
2.1. Introduction ..... 30
**2.2. Ultra-Wideband Signal Model** ..... 32
**2.3. Backprojection Based Stationary and Moving Target Localization** ..... 36
**2.4. CS Based Stationary and Moving Target Localization** ..... 37
2.4.1. Linear Model Formulation ..... 38
2.4.2. CS Data Acquisition and Scene Reconstruction ..... 39
**2.5. Experimental Results** ..... 41
2.5.1. Scene Reconstruction without Time Gating ..... 43
2.5.2. Scene Reconstruction after Time Gating ..... 44
2.5.3. Computational Complexity ..... 45
**2.6. Conclusion** ..... 45
**2.7. References** ..... 46
**Chapter 3 Partially Sparse Reconstruction of Behind-the-Wall Scenes** ..... 59
**3.1. Introduction** ..... 59
**3.2. Partially Sparse Signal Model** ..... 61
**3.3. Partially Sparse Reconstruction** ..... 64
**3.4. Experimental Results** ..... 66
3.4.1. CS Measurement Strategy and Windowing for Enhanced Sparsity ..... 66
3.4.2. Experimental Setup ..... 68
3.4.3. Scene Reconstruction Results ..... 68
**3.5. Conclusion** ..... 70
**3.6. References** ..... 70

## Executive Summary

This report presents research work performed under grant no. N00014-11-1-0576 with the Office of Naval Research over the period of May 2011 to September 2012. It includes contributions from Prof. Moeness Amin (PI), Dr. Fauzia Ahmad (Research Associate Prof.), Dr. Jiang Qian (Postdoctoral Fellow), and Ms. Eva Lagunas (Visiting Scholar). The report consists of three chapters. Each chapter has its own abstract and introduction, and also has its own equation numbers, figure numbers, and references.

In Chapter 1, we consider sparsity-driven change detection for human motion indication in through-the-wall radar imaging (TWRI) and urban sensing applications. Stationary targets and clutter are removed via change detection, which converts a populated scene into a sparse scene of a few human targets moving inside enclosed structures and behind walls. We establish appropriate change detection models for various possible human motions, ranging from translational motions to sudden short movements of the limbs, head, and/or torso. These models permit scene reconstruction within the compressive sensing (CS) framework. Results based on laboratory experiments show that a sizable reduction in the data volume is achieved using the proposed approach without a degradation in system performance.

In Chapter 2, we consider sparsity-driven joint localization of stationary and moving targets inside enclosed structures using a reduced set of spatial-fast time-slow time observations in ultra-wideband (UWB) pulsed radar platforms. We exploit the compact temporal support of the UWB signal to suppress the front wall clutter through time gating. The resulting enhancement in the signal-to-clutter ratio enables application of CS for scene reconstruction. We establish an appropriate signal model that permits formulation of linear modeling with sensing matrices, so as to achieve efficient CS-based localization of stationary and moving targets in the downrange-

crossrange-velocity space. We demonstrate the effectiveness of the proposed scheme using real data collected in a laboratory environment.

In Chapter 3, we apply the idea of partial sparsity to scene reconstruction associated with TWRI of stationary targets. Partially sparse recovery considers the case when it is known a priori that the scene being imaged consists of two parts, one of which is sparse and the other is expected to be dense. More specifically, we consider the scene reconstruction problem involving a few stationary targets of interest when the building layout is assumed known. This implies that the support of the dense part of the image corresponding to the exterior and interior walls is known a priori. This knowledge may be available either through building blueprints or from prior surveillance operations. Using experimental data collected in a laboratory environment, we demonstrate the effectiveness of the partially sparse reconstruction of stationary through-the-wall scenes.

In addition to the aforementioned contributions described in Chapters 1 to 3, two other important challenges faced by CS in urban sensing applications were also addressed. These contributions are summarized below.

Compressive sensing for urban operations and through-the-wall radar imaging has been shown to be successful in fast data acquisition and moving target localizations. The research in this area thus far has assumed effective removal of wall electromagnetic (EM) backscatterings prior to CS application. Wall clutter mitigation can be achieved using full data volume which is, however, in contradiction with the underlying premise of CS. We enable joint wall clutter mitigation and CS application using a reduced set of spatial-frequency observations in stepped frequency radar platforms. Specifically, we demonstrate that wall mitigation techniques, such as spatial filtering and subspace projection, can proceed using fewer measurements. We consider

both cases of having the same reduced set of frequencies at each of the available antenna locations and also when different frequency measurements are employed at different antenna locations. The latter casts a more challenging problem, as it is not amenable to wall removal using direct implementation of filtering or projection techniques. In this case, we apply CS at each antenna individually to recover the corresponding range profile and estimate the scene response at all frequencies. In applying CS, we use prior knowledge of the wall standoff distance to speed up the convergence of the Orthogonal Matching Pursuit for sparse data reconstruction. Real data are used for validation of the proposed approach.

We consider imaging of the building interior structures using Compressive Sensing (CS) with applications to TWRI and urban sensing. We consider a monostatic synthetic aperture radar imaging system employing stepped frequency waveform. The proposed approach exploits prior information of building construction practices to form an appropriate sparse representation of the building interior layout. We devise a dictionary of possible wall locations, which is consistent with the fact that interior walls are typically parallel or perpendicular to the front wall. The dictionary accounts for the dominant normal angle reflections from exterior and interior walls for the monostatic imaging system. CS is applied to a reduced set of observations to recover the true positions of the walls. Additional information about interior walls can be obtained using a dictionary of possible corner reflectors, which is the response of the junction of two walls. Supporting results based on simulation and laboratory experiments are provided. It is shown that the proposed sparsifying basis outperforms the conventional through-the-wall CS model, the wavelet sparsifying basis, and the block sparse model for building interior layout detection.

## List of Publications


[1] F. Ahmad and M. G. Amin, "Through-the-Wall Human Motion Indication using Sparsity-Driven Change Detection," *IEEE Transactions on Geoscience and Remote Sensing*, vol. 51, no. 2, pp. 881-890, Feb. 2013.

[2] E. Lagunas, M. G. Amin, F. Ahmad, and M. Nájar, "Determining building interior structures using compressive sensing," *SPIE/IS&T Journal of Electronic Imaging*, vol. 22, no. 2, Apr. 2013.

[3] J. Qian, F. Ahmad, and M. G. Amin, "Joint Localization of Stationary and Moving Targets behind Walls using Sparse Scene Recovery," *SPIE/IS&T Journal of Electronic Imaging*, vol. 22, no. 2, Apr. 2013.

[4] E. Lagunas, M. G. Amin, F. Ahmad, and M. Nájar, "Joint Wall Mitigation and Compressive Sensing for Indoor Image Reconstruction," *IEEE Transactions on Geoscience and Remote Sensing*, vol. 51, no. 2, pp. 891-906, Feb. 2013.

[5] F. Ahmad, M. G. Amin, "Partially Sparse Reconstruction of Behind-the-Wall Scenes," *Proc. SPIE Symposium on Defense, Security, and Sensing, Compressive Sensing Conference*, vol. 8365, Baltimore, MD, April 2012.

[6] E. L. Targarona, M. Amin, F. Ahmad, and M. Nájar, "'Sparsity-based radar imaging of building structures," *Proc. 20th European Signal Processing Conference*, Bucharest, Romania, August 27-31, 2012.

# Chapter 1

# Through-the-Wall Human Motion Indication using Sparsity-Driven Change Detection

## 1.1. Introduction

One of the primary objectives in through-the-wall radar imaging (TWRI) and urban sensing is the detection and localization of human targets [1-7]. Humans belong to the class of animate objects, which is characterized by motion of the body, breathing, and heartbeat. These features make animate objects distinguishable from inanimate objects and allow the detection of targets of interest to proceed based on changes in the phase of the scattered radar signals over successive probing and data observations.

For urban sensing environments, changes in the backscattered signal phase due to human motion do not necessarily lend themselves to Doppler frequency shifts. This is because the human motion can be abrupt and highly nonstationary, producing a time-dependent phase whose rate of change may fail to translate into a single Doppler shift or multi-component sinusoids that can be captured by different Doppler filters. Instead, the corresponding wide spectrum of human motions becomes non-localizable and can span the entire radar frequency band. In lieu of Doppler filters, time- frequency processing can be applied to reveal the instantaneous frequency signatures [8-10]. However, apart from regularized motions, such as walking and running, time-frequency Doppler signal representations are often very complex and difficult to interpret, especially when dealing with non-homogeneous walls. Therefore, the application of Doppler and micro-Doppler filters for indoor target surveillance may not be a viable option.

Change Detection (CD) can be used in lieu of Doppler processing, wherein human detection is accomplished by subtraction of data frames acquired over successive probing of the scene. CD in TWRI has been discussed in the recent literature, both in the context of moving target

indication [3, 11-15] and background subtraction to detect stationary targets using data acquired during interrogations of a scene at two different time instants [15, 16]. Target detection in through-the-wall radar applications is, in general, a very challenging problem, given the level of multipath and clutter that can contaminate the radar image and the overwhelming return from the front wall that tends to obscure the nearby indoor targets. For stationary target detection, CD requires availability of a reference (background) dataset without the targets, which is very difficult to obtain in practice. Target motion, on the other hand, allows easy access to a reference dataset through multiple interrogations of the scene.

For moving targets, change detection mitigates the heavy clutter that is caused by strong reflections from exterior and interior walls and also removes stationary objects present in the enclosed structure, thereby rendering a densely populated scene sparse [3, 14, 17]. As a result, it becomes possible and more convenient to exploit compression in data collections and processing. Efficient data acquisition and processing enables achieving situational awareness in a quick and reliable manner, which is highly desirable in TWRI and urban sensing applications. The capability of the emerging compressive sensing (CS) techniques to reconstruct a sparse signal from far fewer non-adaptive measurements provides a new perspective for data reduction in radar imaging without compromising the imaging quality [18-21]. The application of CS for TWRI was first reported in [22]. CS techniques can improve the efficacy of the urban sensing operations by reducing the number of antenna elements and/or the number of time samples or frequency steps, depending on the choice of the transmit waveform, culminating in quick turnaround, reliable, and actionable intelligence [22-24].

In this Chapter, we consider sparsity-based change detection in imaging radar systems, aiming at detection and localization of human targets inside buildings, while simultaneously

achieving a sizable reduction in the data volume. CD is first used for stationary background removal. Rather than operating on successive pulses, CD is applied to different data frames for each range bin in the unambiguous range. It is noted that the frames can be consecutive, dealing with targets exhibiting sudden short motions, or nonconsecutive, with relatively long time difference, for the case in which the target changes its range gate position. Scene reconstruction is then achieved using sparsity-driven imaging. We focus on human targets undergoing translational motion as well as sudden short movements of their limbs, heads, and/or torsos. The latter is a typical situation underlying the activities in homes, lecture halls, and auditoriums as well as other sit-down human interactions. For each type of motion, we establish an appropriate change detection model that permits formulation of linear modeling with sensing matrices, so as to apply compressive sensing for scene reconstruction.

Supporting examples based on real data collected in a laboratory environment, using the Radar Imaging facility at the Center for Advanced Communications, Villanova University, are provided. We use an imaging system with a physical aperture. Single target sparse scenes are imaged with the human undergoing both translation and short sudden movement of the head. For both types of human motions, it is shown that, compared to the conventional backprojection-based change detection, the sparsity-driven change detection achieves substantial reduction in the data volume without any degradation in the system performance. The scene reconstructions obtained with the sparsity-based CD not only accurately localize the target undergoing motion, but are also far less cluttered than the conventional reconstructions.

The chapter is organized as follows. In Section 1.2, we describe the signal model and change detection for conventional backprojection-based scene reconstruction. We discuss the sparsity-driven change detection schemes under translational and abrupt human motions in Sections 1.3

and 1.4, respectively, highlighting the key equations. Section 1.5 presents experimental results, comparing the performance of backprojection-based CD and sparsity-based CD using real data of human motion behind a cement board wall. Section 1.6 contains the concluding remarks.

## 1.2. Backprojection-based Change Detection

We first develop the signal model for wideband radar operation with $M$ transmitters and $N$ receivers. A sequential multiplexing of the transmitters with simultaneous reception at multiple receivers is assumed. Although this signaling approach demands more acquisition time compared to the simultaneous transmitter operation, it is a viable option for TWRI operations. This is because a) More receivers than transmitters are deployed due to the important constraint of low cost, and b) The targets of interest move at low velocities indoors. As a result, loss of coherence of the target response may not be an issue. It is important to note that the sequential transmit operation is the salient feature of three known through-the-wall radar imaging systems; one is built by the Army Research Lab [3, 25], the other by the Defense Research and Development Canada [26], and the third by MIT Lincoln Lab [13]. With the assumption of sequential multiplexing, a signal model can thus be developed based on single active transmitters. We note that the timing interval for each data frame is assumed to be a fraction of a second so that the moving target appears stationary during each data collection interval.

Let $s(t)$ be the wideband baseband signal used for interrogating the scene. For the case of a single point target, located at $\mathbf{x}_p = (x_p, y_p)$, the pulse emitted by the $m$th transmitter with phase center at $\mathbf{x}_{tm} = (x_{tm}, 0)$ is received at the $n$th receiver with phase center at $\mathbf{x}_{rn} = (x_{rn}, 0)$ in the form

$$z_{mn}(t) = a_{mn}(t) + b_{mn}(t), \quad a_{mn}(t) = \sigma_p s(t - \tau_{p,mn}) \exp(-j\omega_c \tau_{p,mn}) \tag{1}$$

where $\sigma_p$ is the complex reflectivity of the target, which is assumed to be independent of frequency and aspect angle, $\omega_c$ is the carrier frequency, $\tau_{p,mn}$ is the propagation delay for the signal to travel between the *m*th transmitter, the target at $\mathbf{x}_p$, and the *n*th receiver, and $b_{mn}(t)$ represents the contribution of the stationary background at the *n*th receiver with the *mth* transmitter active. For through-the-wall propagation, $\tau_{p,mn}$ will comprise the components corresponding to traveling distances before, through, and after the wall [27, 28]. Note that the expression in (1) does not consider the wall attenuation and free-space path loss encountered by the radar return. In case of two targets of equal reflectivity located at different distances from the radar system, these losses cause the distant target to appear weaker than the closer target in the image. The wall attenuation and path loss can be easily accommodated in (1) through the use of a scaling factor [20]. However, for notational convenience, we chose to ignore these losses in the problem formulation.

In its simplest form, change detection is achieved by coherent subtraction of the data corresponding to two data frames, which may be consecutive or separated by one or more data frames. This subtraction operation is performed for each range bin. CD results in the set of difference signals, given by,

$$\delta z_{mn}(t) = z_{mn}^{(L+1)}(t) - z_{mn}^{(1)}(t) = a_{mn}^{(L+1)}(t) - a_{mn}^{(1)}(t) \tag{2}$$

where $L$ denotes the number of frames between the two time acquisitions. The component of the radar return from the stationary background is the same over the two time intervals, and is thus removed from the difference signal. We assume that the clutter bandwidth is zero and it is confined to the zero Doppler frequency. It is noted that $L = 1$ represents the case when the two

acquisitions are performed over consecutive frames. Using (1) and (2), the ($m$, $n$)-th difference signal can be expressed as,

$$\delta z_{mn}(t) = \sigma_p s(t - \tau_{p,mn}^{(L+1)}) \exp(-j\omega_c \tau_{p,mn}^{(L+1)}) - \sigma_p s(t - \tau_{p,mn}^{(1)}) \exp(-j\omega_c \tau_{p,mn}^{(1)}) \qquad (3)$$

where $\tau_{p,mn}^{(1)}$ and $\tau_{p,mn}^{(L+1)}$ are the respective two-way propagation delays for the signal to travel between the $m$th transmitter, the target, and the $n$th receiver, during the first and the second data acquisitions, respectively.

In order to generate an image of the scene being interrogated, the $MN$ difference signals corresponding to the operation of $M$ transmitters and $N$ receivers are processed as follows. The region of interest is divided into a finite number of grid points in $x$ and y, where $x$ and $y$ represent crossrange and downrange, respectively. The composite signal corresponding to the pixel, located at $\mathbf{x}_q = (x_q, y_q)$, is obtained by summing time delayed versions of the $MN$ difference signals,

$$\delta z_q(t) = \sum_{m=0}^{M-1} \sum_{n=0}^{N-1} \delta z_{mn}(t + \tau_{q,mn}) = \sum_{m=0}^{M-1} \sum_{n=0}^{N-1} (a_{mn}^{(L+1)}(t + \tau_{q,mn}) - a_{mn}^{(1)}(t + \tau_{q,mn})) \qquad (4)$$

where $\tau_{q,mn}$ is the focusing delay applied to the ($m$, $n$)-th difference signal. It is noted that additional weighting can be applied during the summation operations of (4) to control the sidelobe level of the system point spread function [27, 28]. Substituting from (3) in (4) yields,

$$\begin{aligned} \delta z_q(t) = \sum_{m=0}^{M-1} \sum_{n=0}^{N-1} \sigma_p (s(t + \tau_{q,mn} - \tau_{p,mn}^{(L+1)}) \exp(-j\omega_c (\tau_{p,mn}^{(L+1)} - \tau_{q,mn})) - \\ s(t + \tau_{q,mn} - \tau_{p,mn}^{(1)}) \exp(-j\omega_c (\tau_{p,mn}^{(1)} - \tau_{q,mn}))) \end{aligned} \qquad (5)$$

The complex amplitude image value $I(\mathbf{x}_q)$ for the pixel at $\mathbf{x}_q$ is then obtained by applying a filter, matched to $s(t)$, to $\delta z_q(t)$ and sampling the filtered data, as per the following equation,

$$I(\mathbf{x}_q) = \delta z_q(t) * h(t)\Big|_{t=0} \tag{6}$$

where $h(t) = s^*(-t)$ is the impulse response of the matched filter, the superscript '*' denotes complex conjugation, and '*' denotes the convolution operator. The process described by (4)-(6) is repeated for all pixels in the image to generate the composite image of the scene. The general case of multiple targets can be obtained by superposition of target reflections [27, 28].

Normally, we work with discrete versions of the measured time signals. Note that not all time samples of the difference signal are necessary to obtain the corresponding image. Even if some of the data samples are missing, information on the moving targets in the field of view can still be obtained. However, merely employing part of the signal time duration in backprojection provides an image quality that is degraded in proportion to the number of missing data [29]. Since the removal of stationary background converts a populated scene into a sparse scene of moving targets, reduction in data volume should be pursued under the CS framework.

### 1.3. Sparsity-Driven Change Detection under Translational Motion

Consider the difference signal in (3), reproduced below for convenience, for the case where the target is undergoing translational motion. Two nonconsecutive data frames with relatively long time difference are used, i.e., $L >> 1$.

$$\delta z_{mn}(t) = \sigma_p s(t - \tau_{p,mn}^{(L+1)}) \exp(-j\omega_c \tau_{p,mn}^{(L+1)}) - \sigma_p s(t - \tau_{p,mn}^{(1)}) \exp(-j\omega_c \tau_{p,mn}^{(1)}) \tag{7}$$

In this case, the target will change its range gate position during the time elapsed between the two data acquisitions. As seen from (7), the moving target will present itself as two targets, one corresponding to the target position during the first time interval and the other corresponding to the target location during the second data frame. It is noted that the imaged target at the reference position corresponding to the first data frame cannot be suppressed for the coherent change

detection approach, whether employing backprojection or sparsity-driven imaging. On the other hand, the noncoherent CD approach that deals with differences of image magnitudes corresponding to the two data frames, allows suppression of the reference image through a zero thresholding operation [14]. However, as the noncoherent approach requires the scene reconstruction to be performed prior to change detection, it is not a feasible option for sparsity-based imaging, which relies on coherent CD to render the scene sparse. Therefore, we rewrite (7) as,

$$\delta z_{mn}(t) = \sum_{i=1}^{2} \tilde{\sigma}_i s(t - \tau_{i,mn}) \exp(-j\omega_c \tau_{i,mn}) \tag{8}$$

with

$$\tilde{\sigma}_i = \begin{cases} \sigma_p & i = 1 \\ -\sigma_p & i = 2 \end{cases} \quad \text{and} \quad \tau_{i,mn} = \begin{cases} \tau_{p,mn}^{(L+1)} & i = 1 \\ \tau_{p,mn}^{(1)} & i = 2 \end{cases} \tag{9}$$

Assume that the scene being imaged, or the target space, is divided into a finite number of grid-points in crossrange and downrange. If we sample the difference signal $\delta z_{mn}(t)$ at times $\{t_k\}_{k=0}^{K-1}$ to obtain the $K\times 1$ vector $\mathbf{\Delta z}_{mn}$ and form the concatenated $Q\times 1$ scene reflectivity vector $\tilde{\boldsymbol{\sigma}}$ corresponding to the spatial sampling grid, then using the developed signal model in (9), we obtain the linear system of equations [20, 22, 24],

$$\mathbf{\Delta z}_{mn} = \boldsymbol{\Psi}_{mn} \tilde{\boldsymbol{\sigma}} \tag{10}$$

The $q$th column of $\boldsymbol{\Psi}_{mn}$ consists of the received signal corresponding to a target at grid point $\mathbf{x}_q$ and the $k$th element of the $q$th column can be written as [20]

$$[\boldsymbol{\Psi}_{mn}]_{k,q} = \frac{s(t_k - \tau_{q,mn}) \exp(-j\omega_c \tau_{q,mn})}{\left\| \mathbf{s}_{q,mn} \right\|_2}, k = 0,1,\ldots,K\text{-}1,\ q = 0,1,\ldots,Q-1 \tag{11}$$

where $\tau_{q,mn}$ is the two-way signal traveling time from the $m$th transmitter to the $q$th grid point and back to the $n$th receiver. Note that the $k$th element of the vector $\mathbf{s}_{q,mn}$ is $s(t_k - \tau_{q,mn})$, which implies that the denominator in the R.H.S. of (11) is the energy in the time signal. Therefore, each column of $\mathbf{\Psi}_{mn}$ has unit norm. Further note that $\tilde{\boldsymbol{\sigma}}$ in (10) is a weighted indicator vector defining the scene reflectivity, i.e., if there is a target at the $q$th grid point, the value of the $q$th element of $\tilde{\boldsymbol{\sigma}}$ should be $\tilde{\sigma}_q$; otherwise, it is zero.

The change detection model described in (10-11) permits the scene reconstruction within the compressive sensing framework. We measure an $L(< K)$ dimensional vector of elements randomly chosen from $\Delta\mathbf{z}_{mn}$. The new measurements can be expressed as

$$\xi_{mn} = \mathbf{\Phi}_{mn}\Delta\mathbf{z}_{mn} = \mathbf{\Phi}_{mn}\mathbf{\Psi}_{mn}\tilde{\boldsymbol{\sigma}} \tag{12}$$

where $\mathbf{\Phi}_{mn}$ is an $L\times K$ measurement matrix. Several types of measurement matrices have been reported in the literature [20, 21, 30 and the references therein]. To name a few, a measurement matrix whose elements are drawn from a Gaussian distribution, a measurement matrix having random ±1 entries with probability of 0.5, or a random matrix whose entries can be constructed by randomly selecting rows of a $K\times K$ identity matrix. It was shown in [20] that the measurement matrix with random ±1 elements requires the least amount of compressive measurements for the same radar imaging performance, and permits a relatively straight forward data acquisition implementation. Therefore, we choose to use such a measurement matrix in image reconstructions.

Given $\xi_{mn}$ for $m = 0,1,\ldots,M-1$, $n = 0,1,\ldots,N-1$, we can recover $\tilde{\boldsymbol{\sigma}}$ by solving the following equation,

$$\hat{\tilde{\boldsymbol{\sigma}}} = \arg\min_{\tilde{\boldsymbol{\sigma}}} \left\| \tilde{\boldsymbol{\sigma}} \right\|_{l_1} \text{ subject to } \boldsymbol{\Phi\Psi}\tilde{\boldsymbol{\sigma}} \approx \boldsymbol{\xi} \tag{13}$$

where

$$\begin{aligned} &\boldsymbol{\Psi} = [\boldsymbol{\Psi}_{00}^T \; \boldsymbol{\Psi}_{01}^T \ldots \boldsymbol{\Psi}_{(M-1)(N-1)}^T]^T, \quad \boldsymbol{\Phi} = diag(\boldsymbol{\Phi}_{00}, \boldsymbol{\Phi}_{01}, \ldots, \boldsymbol{\Phi}_{(M-1)(N-1)}) \\ &\boldsymbol{\xi} = [\boldsymbol{\xi}_{00}^T \; \boldsymbol{\xi}_{01}^T \cdots \boldsymbol{\xi}_{(M-1)(N-1)}^T]^T \end{aligned} \tag{14}$$

A stable solution of the sparse target space reconstruction problem in (13) is guaranteed provided that the product matrix $\boldsymbol{\Phi\Psi}$ satisfies the Restricted Isometry Property (RIP), which states that all subsets of $r$ columns taken from $\boldsymbol{\Phi\Psi}$ are, in fact, nearly orthogonal, $r$ being the sparsity of the signal $\tilde{\boldsymbol{\sigma}}$ [20, 21, 31]. A measurement matrix $\boldsymbol{\Phi}$, whose elements are independent, identically distributed Bernoulli or Gaussian random variables, has been shown to satisfy the RIP with matrix $\boldsymbol{\Psi}$ resulting from sinusoids, wavelets, Gabor functions, etc. [32]. In general, it is computationally difficult to check this property and, therefore, other related measures on the product matrix $\boldsymbol{\Phi\Psi}$, such as mutual coherence, are often used to guarantee stable recovery through $l_1$-minimization [21]. Mutual coherence of the columns of $\boldsymbol{\Phi\Psi}$ can be viewed as the largest off-diagonal entry of the Gram matrix $(\boldsymbol{\Phi\Psi})^H(\boldsymbol{\Phi\Psi})$, where the columns of $\boldsymbol{\Phi\Psi}$ have been normalized. The matrix $\boldsymbol{\Phi\Psi}$ is considered to be incoherent if the value of the mutual coherence is small. We will address the mutual coherence of the product matrix $\boldsymbol{\Phi\Psi}$ used in the experimental results in Section 1.5. We note that the problem in (13) can be solved using convex relaxation, greedy pursuit, or combinatorial algorithms [31, 33, 34]. In this work, we choose CoSaMP as the reconstruction algorithm primarily because of its ability to handle complex arithmetic [33].

Equations (13, 14) represent one strategy that can be adopted for sparsity-based change detection approach, wherein a reduced number of time samples are chosen randomly for all the

transmitter-receiver pairs constituting the array apertures. The above two equations can also be extended so that the reduction in data measurements includes both spatial and time samples [20, 22]. The latter strategy is not considered in this Chapter.

### 1.4. Sparsity-Driven Change Detection under Short Sudden Movement

Assume that consecutive ($L$=1) data frames are employed for change detection and consider a scene comprising a human target undergoing sudden short movements of the limbs, head, and/or torso. That is, only a small portion of the body moves but remains within the same resolution cell. In this case, we can model the target as a cluster of $P$ point scatterers within the same resolution cell and only a small number, say $P_1$, of these scatterers moves during successive data acquisitions. For example, in a round-the-table meeting, the upper part of the human body, especially the hands, is likely to move while the legs remain stationary over successive observations. Using (1), the baseband received signal, corresponding to the ($m$, $n$)-th transmitter-receiver pair, for the first data frame can be expressed as,

$$z_{mn}^{(1)}(t) = \sum_{p=1}^{P} \sigma_p s(t - \tau_{p,mn}^{(1)}) \exp(-j\omega_c \tau_{p,mn}^{(1)}) + b_{mn}(t) \tag{15}$$

where $\sigma_p$ is the complex reflectivity of the $p$th point scatterer, and $\tau_{p,mn}^{(1)}$ is the two-way propagation delay for the signal to travel between the ($m$, $n$)-th transmitter-receiver pair and the $p$th scatterer during the first frame. As the $P$ scatterers are clustered within the same resolution cell, we can rewrite (15) as,

$$z_{mn}^{(1)}(t) = \sigma_{mn}^{(1)} s(t - \bar{\tau}_{mn}) \exp(-j\omega_c \bar{\tau}_{mn}) + b_{mn}(t) \tag{16}$$

where $\bar{\tau}_{mn}$ is the propagation delay from the $m$th transmitter to the center of the cell and back to the $n$th receiver, and

$$\sigma_{mn}^{(1)} = \sum_{p=1}^{P} \sigma_p \exp(-j\omega_c \Delta\tau_{p,mn}^{(1)}) \tag{17}$$

is the net target reflectivity with $\Delta\tau_{p,mn}^{(1)} = \tau_{p,mn}^{(1)} - \bar{\tau}_{mn}$.

Let the first $P_1$ scatterers represent the portion of the body that undergoes a short movement. Then, the $m$th received signal corresponding to the second data frame can be expressed as,

$$z_{mn}^{(2)}(t) = \sigma_{mn}^{(2)} s(t - \bar{\tau}_{mn}) \exp(-j\omega_c \bar{\tau}_{mn}) + b_{mn}(t) \tag{18}$$

with the net reflectivity $\sigma_{mn}^{(2)}$ given by,

$$\sigma_{mn}^{(2)} = \sum_{p=1}^{P_1} \sigma_p \exp(-j\omega_c \Delta\tau_{p,mn}^{(2)}) + \sum_{p=P_1+1}^{P} \sigma_p \exp(-j\omega_c \Delta\tau_{p,mn}^{(1)}) \tag{19}$$

and the set of differential delays, $\left\{\Delta\tau_{p,mn}^{(2)} = \tau_{p,mn}^{(2)} - \bar{\tau}_{mn}\right\}_{p=1}^{P_1}$, corresponds to the new locations of the $P_1$ scatterers within the same resolution cell. The difference signal corresponding to these successive data measurements is given by,

$$\delta z_{mn}(t) = z_{mn}^{(2)}(t) - z_{mn}^{(1)}(t) = (\sigma_{mn}^{(2)} - \sigma_{mn}^{(1)}) s(t - \bar{\tau}_{mn}) \exp(-j\omega_c \bar{\tau}_{mn}) = \delta\sigma_{mn} s(t - \bar{\tau}_{mn}) \exp(-j\omega_c \bar{\tau}_{mn}) \tag{20}$$

where $\delta\sigma_{mn}$ represents the change in reflectivity between the consecutive acquisitions.

Again, working with a discretized version of (20) and for the target space consisting of $Q$ grid-points in crossrange and downrange, we obtain the linear system of equations,

$$\Delta\mathbf{z}_{mn} = \boldsymbol{\Psi}_{mn} \delta\boldsymbol{\sigma}_{mn} \tag{21}$$

where $\boldsymbol{\Psi}_{mn}$ is defined in (11) and $\delta\boldsymbol{\sigma}_{mn}$ is a weighted indicator vector defining the change in scene reflectivity as observed at the $n$th receiver with the $m$th transmitter active, i.e., if there is a

change in target reflectivity at the $q$th grid point, the value of the $q$th element of $\boldsymbol{\delta\sigma}_{mn}$ will be $\sigma^{(2)}_{q,mn} - \sigma^{(1)}_{q,mn}$ and zero otherwise.

For the signal model in (21), we observe that the change in scene reflectivity depends on the transmitter and receiver locations. As such, the aspect-independent scattering assumption is no longer applicable and there exists a map of the change in scene reflectivity for each transmitter-receiver pair. To address this issue of limited persistence in the change in target reflectivity across the various transmit-receive pairs, we consider composite image formation using sub-apertures [35]. In this scheme, the transmit and receive arrays are divided into sub-apertures. Assuming isotropic scattering within the angular extent of these sub-apertures, sub-images can be obtained, which are then combined to form a single composite image of the scene. The sub-aperture based scene reconstruction can be performed within the CS framework using the change detection model of (21).

Assume the $M$-element transmit and the $N$-element receive arrays are divided into $K_1$ and $K_2$ non-overlapping sub-apertures, respectively. The choice of $K_1$ and $K_2$ is guided by the local isotropy requirement, i.e., each transmit and receive sub-aperture should correspond to a small aspect angle dataset (typically on the order of a few degrees). In the spirit of CS, a small number of "random" measurements carry enough information to completely represent the sparse signal $\boldsymbol{\delta\sigma}^{(k_1,k_2)}$, which is the 'image' of the scene corresponding to the $k_1$th transmit and the $k_2$th receive sub-apertures. Thus, we measure a random subset of $L$ ($< K$) samples of the difference signal for the $n_{k_2}$ th antenna of the $k_2$th receive sub-aperture when the $m_{k_1}$ th antenna of the $k_1$th transmit sub-aperture is active. In matrix form, the new measurements can be expressed as

$$\boldsymbol{\xi}^{(k_1,k_2)}_{m_{k_1}n_{k_2}} = \boldsymbol{\Phi}^{(k_1,k_2)}_{m_{k_1}n_{k_2}} \Delta\mathbf{z}^{(k_1,k_2)}_{m_{k_1}n_{k_2}} = \boldsymbol{\Phi}^{(k_1,k_2)}_{m_{k_1}n_{k_2}} \boldsymbol{\Psi}^{(k_1,k_2)}_{m_{k_1}n_{k_2}} \boldsymbol{\delta\sigma}^{(k_1,k_2)} \tag{22}$$

where $\mathbf{\Phi}_{m_{k_1} n_{k_2}}^{(k_1,k_2)}$ is an $L \times K$ measurement matrix corresponding to the $n_{k_2}$ th antenna position in the $k_2$th receive sub-aperture and the $m_{k_1}$ th antenna in the $k_1$th transmit sub-aperture. Given $\xi_{m_{k_1} n_{k_2}}^{(k_1,k_2)}$ for $m_{k_1} = 0,1,\ldots,\lceil M/K_1 \rceil - 1, n_{k_2} = 0,1,\ldots,\lceil N/K_2 \rceil - 1$, we can recover $\delta\boldsymbol{\sigma}^{(k_1,k_2)}$ by solving the following equation,

$$\delta\hat{\boldsymbol{\sigma}}^{(k_1,k_2)} = \arg\min_{\boldsymbol{\alpha}} \|\boldsymbol{\alpha}\|_1 \text{ subject to } \mathbf{\Phi}^{(k_1,k_2)} \mathbf{\Psi}^{(k_1,k_2)} \boldsymbol{\alpha} \approx \boldsymbol{\xi}^{(k_1,k_2)} \tag{23}$$

where

$$\begin{aligned}
\mathbf{\Psi}^{(k_1,k_2)} &= [(\mathbf{\Psi}_{00}^{(k_1,k_2)})^T \, (\mathbf{\Psi}_{01}^{(k_1,k_2)})^T \ldots (\mathbf{\Psi}_{\lceil M/K_1 \rceil - 1, \lceil N/K_2 \rceil - 1}^{(k_1,k_2)})^T]^T, \\
\mathbf{\Phi}^{(k_1,k_2)} &= diag(\mathbf{\Phi}_{00}^{(k_1,k_2)} \, \mathbf{\Phi}_{01}^{(k_1,k_2)} \ldots \mathbf{\Phi}_{\lceil M/K_1 \rceil - 1, \lceil N/K_2 \rceil - 1}^{(k_1,k_2)}) \\
\xi^{(k_1,k_2)} &= [(\xi_{00}^{(k_1,k_2)})^T \, (\xi_{01}^{(k_1,k_2)})^T \ldots (\xi_{\lceil M/K_1 \rceil - 1, \lceil N/K_2 \rceil - 1}^{(k_1,k_2)})^T]^T
\end{aligned} \tag{24}$$

Once the sub-images $\delta\hat{\boldsymbol{\sigma}}^{(k_1,k_2)}$ corresponding to all $K_1$ transmit and $K_2$ receive sub-apertures have been reconstructed, the composite image $\delta\hat{\boldsymbol{\sigma}}$ can be formed as

$$[\delta\hat{\boldsymbol{\sigma}}]_q = \arg\max_{k_1,k_2} \left| [\delta\hat{\boldsymbol{\sigma}}^{(k_1,k_2)}]_q \right| \tag{25}$$

where $[\delta\hat{\boldsymbol{\sigma}}]_q$ and $[\delta\hat{\boldsymbol{\sigma}}^{(k_1,k_2)}]_q$ denote the $q$th pixel of the composite image and the sub-image corresponding to the $k_1$th transmit and $k_2$th receive sub-apertures, respectively. Alternatively, the sub-aperture image combining can be achieved using

$$[\delta\hat{\boldsymbol{\sigma}}]_q = \sum_{k_1=1}^{K_1} \sum_{k_2=1}^{K_2} \left| [\delta\hat{\boldsymbol{\sigma}}^{(k_1,k_2)}]_q \right|. \tag{26}$$

The expression in (25) performs a nonlinear combination of the pixel magnitudes of the sub-images, whereas (26) forms the composite image through a linear combination of the sub-aperture images.

It is noted that the model and reconstruction approach presented here for short sudden movements of the human target are also applicable to translational motion for the case when two consecutive measurements are used for change detection. In this case, similar to short sudden movements, only a small part of the body moves; however, unlike the short movements, the body part may move into the next resolution cell. This will lead to changes in scene reflectivity for both resolution cells.

### 1.5. Experimental Results

A through-the-wall wideband pulsed radar system was used for real data collection in the Radar Imaging Lab at Villanova University. The system uses a 0.7ns pulse, shown in Fig. 1, for scene interrogation. The pulse is up-converted to 3 GHz for transmission and down-converted to baseband through in-phase and quadrature demodulation on reception. The system operational bandwidth from 1.5 – 4.5 GHz provides a range resolution of 5cm. The peak transmit power is 25dBm. Transmission is through a single horn antenna, model BAE-H1479, with an operational bandwidth from 1 to 12.4 GHz, which is mounted on a tripod. An 8-element line array of Vivaldi elements with an inter-element spacing of 0.06m, is used as the receiver and is placed to the right of the transmit antenna. The center-to-center separation between the transmitter and the leftmost receive antenna is 0.28m, as shown in Fig. 2. A 3.65m × 2.6m wall segment was constructed utilizing 1cm thick cement board on a 2-by-4 wood stud frame. The transmit antenna and the receive array were at a standoff distance of 1.19m from the wall. The pulse repetition frequency (PRF) is 10MHz, providing an unambiguous range of 15m, which is roughly three times the length of the room being imaged. Despite the high PRF, the system refresh rate is 100Hz. This is because a) Equivalent time sampling is used [36], and b) Instead of simultaneous reception, the receive array elements are accessed sequentially through a multiplexer.

In order to illustrate the performance of the sparsity-driven change detection scheme under both translational and sudden short human motions, two different experiments were considered. In the first experiment, a person walked away from the wall in an empty room (the back and the side walls were covered with RF absorbing material) along a straight line path. The path is located 0.5m to the right of the center of the scene, as shown in Fig. 2. The data collection started with the target at position 1 and ended after the target reached position 3, with the target pausing at each position along the trajectory for a second. Consider the data frames corresponding to the target at position 2 and position 3. Each frame consists of 20 pulses, which are coherently integrated to improve the signal-to-noise ratio. The imaging region (target space) is chosen to be 3m × 3m, centered at (0.5m, 4m), and divided into 61 × 61 grid points in corssrange and downrange, resulting in 3721 unknowns. The space-time response of the target space consists of 8 × 1536 space-time measurements. Figure 3(a) shows the backprojection-based CD image of the scene using all 8 × 1536 data points. In this figure and all subsequent figures in this section, we plot the image intensity with the maximum intensity value in each image normalized to 0dB. We observe that, as the human changed its range gate position during the time elapsed between the two data acquisitions, it presents itself as two targets in the image, and is correctly localized at both of its positions.

For sparsity-based CD, only 5% of the 1536 time samples are randomly selected at each of the 8 receive antenna locations, resulting in 8 × 77 space-time measured data. More specifically, the 77 time samples at each receive location were obtained as the product of the 1536 point time-domain response with a 77 × 1536 measurement matrix, whose elements are randomly chosen ±1 values with a probability of ½. According to compressive sensing theory, an $r$-sparse target space with $Q$ unknowns can be recovered from $O(r\log(Q))$ measurements [37]. The human

target roughly extended 0.5m in crossrange and 0.25m in downrange, thereby occupying 10 x 5 grid points. Therefore, for the dataset under consideration wherein the target presents itself as two targets after change detection, the 8 × 77 measured data points exceed this requirement of $O(r\log(Q))$ measurements. We reconstructed the target space using sparsity-based CD with 5% data volume one hundred times. For each trial, a different random measurement matrix was used to generate the reduced set of measurements, followed by sparsity-based scene reconstruction. For each of the 100 trials, we also computed the mutual coherence of the columns of the product of the measurement matrix $\mathbf{\Phi}$, with random ±1 elemental values, and the $\mathbf{\Psi}$ matrix defined in (14). The average value of the mutual coherence of the corresponding product matrix is equal to 0.892. Figure 3(b) depicts the sparsity-based CD result, averaged over one hundred trials. The higher the intensity of a grid point in this figure, the greater is the number of times that grid point was populated during the 100 reconstruction trials. We observe that, on average, the sparsity-based CD scheme detects and localizes the target accurately at both positions. Also, compared to the backprojection-based result of Fig. 3(a), the image in Fig. 3(b) is less cluttered. The 'cleaner' image is due to the fact that a sparse solution is enforced by the $l_1$ minimization in (13).

To further verify the performance of the sparsity-driven scheme, we computed the rate of successful reconstruction corresponding to the 100 trials for the translation motion. An image was regarded as a successful reconstruction if the pixel with the highest intensity was located within the extent of the target at the first (closer) position and if the second imaged target was populated with at least one pixel of significant intensity. Comparing the intensity of the two imaged targets in the backprojected image, the significant pixel intensity was selected to be within 5 dB of the highest intensity. An example of a successful reconstruction is provided in Fig. 4. Based on these criteria, the successful recovery rate was determined to be 84%.

Next, we collected data from a scene, consisting of a standing human facing the wall, located at 0.5m crossrange and at a downrange of 3.9m from the radar, as shown in Fig. 5. The data was collected with the target initially looking straight at the wall and then suddenly lifting the head to look upwards. As the person moved the head, there was also a slight movement of the shoulders and heaving of the chest. Two data frames of 20 pulses each, corresponding to the two head positions, were considered. The system parameters, the dimensions of the target space, the number of grid points, and the number of space-time measurements employed for the backprojection-based and sparsity-based reconstructions are all the same as those for the translational motion example. The target space image obtained using the backprojection-based CD with full data volume (after coherent integration) is shown in Fig. 6. We observe that the change detection approach was able to detect the cumulative change in target reflectivity due to the head movement and associated slight outward and upward movement of the chest as the target looked upwards. Compared to the translational motion image of Fig. 3(a), the sudden short movement image is more cluttered. This is because the radar return is much weaker in this case due to a slight motion of only a small part of the body.

For the corresponding sparsity-based CD composite imaging results, we used two sub-apertures, each consisting of 4 receive antenna elements, and employed only 5% of the total data volume. That is, we used 77 time samples per antenna location within each of the sub-apertures. Similar to the translational motion example, we performed scene reconstruction one hundred times, and the averaged target space images with the sub-images combined in accordance to (25) and (26) are provided in Figs. 7(a) and 7(b), respectively. We observe that, on average, the two sub-image combining approaches provide comparable performance, and the sparsity-based CD approach successfully detects and localizes the target undergoing short movement using much

reduced data volume. For comparison, the sparsity-based scene reconstruction using the full receive array and 5% data volume, averaged over one hundred trials, is also provided in Fig. 8. We note that although the non-composite image approach, on average, detects the presence of both the head and chest movements, the location of the highest intensity pixel is offset in downrange by about 5cm. Despite this issue, the average performance of the non-composite scheme is reasonable compared to that of the composite imaging approaches. The reason being that the receive array is just 0.42m in length, and the aspect angle variation across the array elements is no more than 6 degrees for the considered target space. Thus, the isotropic scattering assumption is not violated through the use of the full receive array.

For the sudden movement case, we also computed the rate of successful reconstruction corresponding to the 100 trials for the sparsity-based composite image approaches. An image was regarded as a successful reconstruction if the pixel with the highest intensity was located within the extent of the target. Based on this criterion, the respective successful recovery rates for the sub-image combination schemes of (25) and (26) were determined to be 75% and 73%.

## 1.6. Conclusion

In this Chapter, we detected and localized moving humans behind walls and inside enclosed structures using an approach that combines sparsity-driven radar imaging and change detection. Removal of stationary background via change detection converts populated scenes to sparse scenes, whereby compressive sensing schemes can exploit full benefits of sparsity-driven imaging. Both translational motion and short sudden movements of the head, limbs, and/or torso were considered and appropriate change detection models were developed for both motion types that allowed scene reconstruction within the compressive sensing framework. Examples of a human target undergoing translation motion and slight movement of the head behind a cement

board wall were used to validate the developed models and to evaluate the performance of the proposed sparsity-driven change detection scheme. Using pulsed radar operation, it was demonstrated that a sizable reduction in the data volume is achieved by the proposed approach without degradation in system performance.

It is noted that the work presented here only considered the sparsity of the target space and did not make any further assumptions about the support of the sparse solution during the reconstruction process. As the humans are extended targets, they appear as clusters in the through-the-wall images. As such, the corresponding sparse solution support has an underlying block structure [38, 39]. Future efforts will focus on exploiting this structured sparsity to further reduce the number of compressive measurements required for stable recovery.

## 1.7. References


[1] M.G. Amin (Ed.), *Through-the-Wall Radar Imaging,* CRC Press, 2010.

[2] M. Amin and K. Sarabandi (Eds.), Special Issue on Remote Sensing of Building Interior, *IEEE Trans. Geosci. Remote Sens.*, vol. 47, no. 5, pp. 1270-1420, 2009.

[3] A. Martone, K. Ranney, and R. Innocenti, "Automatic through the wall detection of moving targets using low-frequency ultra-wideband radar," in *Proc. IEEE Int. Radar Conf.*, Washington D.C., pp. 39-43, May 2010.

[4] S. S. Ram and H. Ling, "Through-wall tracking of human movers using joint Doppler and array processing," *IEEE Geosci. Remote Sens. Lett.*, vol. 5, no.3, pp. 537-541, 2008.

[5] M. Amin (Guest Editor), Special Issue on "Advances in indoor radar imaging," *J. Franklin Institute*, vol. 345, no. 6, pp. 556-722, 2008.

[6] T. Dogaru and C. Le, "Validation of Xpatch computer models for human body radar signature," U.S. ARL technical report ARL-TR-4403, March 2008.

[7] C. P. Lai and R. M. Narayanan, "Through-wall imaging and characterization of human activity using ultrawideband (UWB) random noise radar," in *Proc. SPIE - Sensors and C3I Technologies for Homeland Security and Homeland Defense*, May 2005, vol. 5778, pp. 186-195.

[8] S. S. Ram, Y. Li, A. Lin, and H. Ling, "Doppler-based detection and tracking of humans in indoor environments," *J. Franklin Inst.*, vol. 345, no. 6, pp. 679-699, 2008.

[9] T. Thayaparan, L. Stankovic, and I. Djurovic, "Micro-Doppler human signature detection and its application to gait recognition and indoor imaging," *J. Franklin Inst.*, vol. 345, no. 6, pp.700-722, 2008.

[10] I. Orovic, S. Stankovic, and M. Amin, "A new approach for classification of human gait based on time-frequency feature representations," *Signal Processing*, vol. 91, no. 6, pp. 1448-1456, 2011.

[11] A. R. Hunt, "Use of a frequency-hopping radar for imaging and motion detection through walls," *IEEE Trans. Geosci. Remote Sens.*, vol. 47, no. 5, pp. 1402-1408, 2009.

[12] N. Maaref, P. Millot, C. Pichot, and O. Picon, "A study of UWB FM-CW Radar for the detection of human beings in motion inside a building," *IEEE Trans. Geosci. Remote Sens.*, vol. 47, no. 5, pp. 1297-1300, 2009.

[13] T. S. Ralston, G. L. Charvat, and J. E. Peabody, "Real-time through-wall imaging using an ultrawideband multiple-input multiple-output (MIMO) phased array radar system," in *Proc. IEEE Intl. Symp. Phased Array Systems and Technology,* Boston, MA, October 2010, pp. 551-558.

[14] M. G. Amin and F. Ahmad, "Change detection analysis of humans moving behind walls," *IEEE Trans. Aerosp. Electron. Syst.,* In Press.

[15] F. Soldovieri, R. Solimene, and R. Pierri, "A simple strategy to detect changes in through the wall imaging," *Progress in Electromagnetics Research M,* vol. 7, pp. 1-13,2009.

[16] J. Moulton, S. A. Kassam, F. Ahmad, M. G. Amin, and K. Yemelyanov, "Target and change detection in synthetic aperture radar sensing of urban structures," in *Proc. IEEE Radar Conf,* Rome, Italy, May 2008.

[17] M. G. Amin, F. Ahmad, W. Zhang, "A compressive sensing approach to moving target indication for urban sensing," in *Proc. IEEE Radar Conf,* Kansas City, MO, May 2011.

[18] R. Baraniuk and P. Steeghs, "Compressive radar imaging," in *Proc. IEEE Radar Conf.,* Waltham, MA, April 2007, pp. 128-133.

[19] M. Herman and T. Strohmer, "High-resolution radar via compressive sensing," *IEEE Trans. Signal Process.,* vol. 57, no. 6, pp. 2275-2284, 2009.

[20] A. Gurbuz, J. McClellan, and W. Scott, Jr., "Compressive sensing for subsurface imaging using ground penetrating radar," *Signal Processing,* vol. 89, no. 10, pp. 1959-1972, 2009.

[21] L. C. Potter, E. Ertin, 1. T. Parker, and M. Cetin, "Sparsity and compressed sensing in radar imaging," *Proc. of the IEEE,* vol. 98, no. 6, pp. 1006-1020, 2010.

[22] Y. Yoon and M. G. Amin, "Compressed sensing technique for high-resolution radar imaging," in *Proc. SPIE,* vol. 6968,2008, pp. 69681A-69681A-I0.

[23] Q. Huang, L. Qu, B. Wu, and G. Fang, "UWB through-wall imaging based on compressive sensing," *IEEE Trans. Geosci. Remote Sens.,* vol. 48, no. 3, pp. 14081415, 2010.

[24] M. Leigsnering, C. Debes, A.M. Zoubir, "Compressive sensing in through-the-wall radar imaging," in *Proc. IEEE Int. Conf. Acoustics, Speech, and Signal Process.,* Prague, Czech Republic, May 2011, pp. 4008-4011.

[25] K. Ranney et al., "Recent MTI experiments using ARL's Synchronous Impulse Reconstruction (SIRE) Radar," in *Proc. SPIE-Radar Sensor Technology XII,* April 2008, vol. 6947, pp. 694708-1-694708-9.

[26] P. Sevigny et al., "Concept of operation and preliminary experimental results of the DRDC through-wall SAR system ," *Proc. SPIE-Radar Sensor Technology XIV,* April 2010, vol. 7669, pp. 766907-1-766907-11.

[27] F. Ahmad, Y. Zhang, and M. G. Amin, "Three-dimensional wideband beamforming for imaging through a single wall," *IEEE Geosci. Remote Sens. Lett.,* vol. 5, no. 2, April 2008.

[28] M. G. Amin and F. Ahmad, "Wideband synthetic aperture beamforming for through-the-wall imaging," *IEEE Signal Process. Mag.,* vol. 25, no. 4, pp. 110-113, Jul. 2008.

[29] L. He, S. A. Kassam, F. Ahmad, and M. G. Amin, "Sparse multi-frequency waveform design for wideband imaging," in *Principles of Waveform Diversity and Design*, M. Wicks, E. Mokole, S. Blunt, R. Schneible, V. Amuso, Eds., SciTech Publishing, 2010, pp. 922-938.

[30] X. X. Zhu and R. Bamler, "Tomographic SAR inversion by $L_1$-norm regularization—The compressive sensing approach," *IEEE Trans. Geosci. Remote Sens.*, vol.48, no.10, pp.3839-3846, Oct. 2010.

[31]E. Candes, J. Romberg and T. Tao, "Stable signal recovery from incomplete and inaccurate measurements," *Communications in Pure and Applied Mathematics,* vol. 59, pp. 1207-1223, 2006.

[32] R. Baraniuk, M. Davenport, R. DeVore, and M. Wakin, "A simple proof of the restricted isometry property for random matrices," *Constructive Approximation*, vol. 28, no. 3, pp. 253-263, Dec. 2008.

[33] D. Needell and J. A. Tropp, "CoSaMP: Iterative signal recovery from incomplete and inaccurate samples," *Appl. Comput. Harmon. Anal.,* vol. 26, no. 3, pp. 301-321, May 2009.

[34] R. Tibshirani, "Regression shrinkage and selection via the LASSO," *J. Royal. Statist. Soc B.*, vol. 58, pp. 267–288, 1996.

[35] M. Cetin and R. L. Moses, "SAR imaging from partial-aperture data with frequency-band omissions," in *Proc. SPIE,* vol. 5808, 2005, pp. 32-43.

[36] Y. Yang and A. Fathy, "Development and implementation of a real-time see-through-wall radar system based on FPGA," *IEEE Trans. Geosci. Remote Sens.*, vol. 47, no. 5, pp. 1270-1280, 2009.

[37]M. T. Alonso, P. López-Dekker, and J. J. Mallorquí, "A novel strategy for radar imaging based on compressive sensing," *IEEE Trans. Geosci. Remote Sens.*, vol.48, no.12, pp.4285-4295, Dec. 2010.

[38] R. G. Baraniuk, V. Cevher, M. F. Duarte, and C. Hegde, "Model-based compressive sensing," *IEEE Trans. Inf. Theory*, vol. 56, no. 4, pp. 1982-2001, 2010.

[39] V. Cevher, P. Indyk, C. Hegde, and R. G. Baraniuk, "Recovery of clustered sparse signals from compressive measurements," in *8th Int. Conf. on Sampling Theory and Applications*, Marseille, France, May 2009.

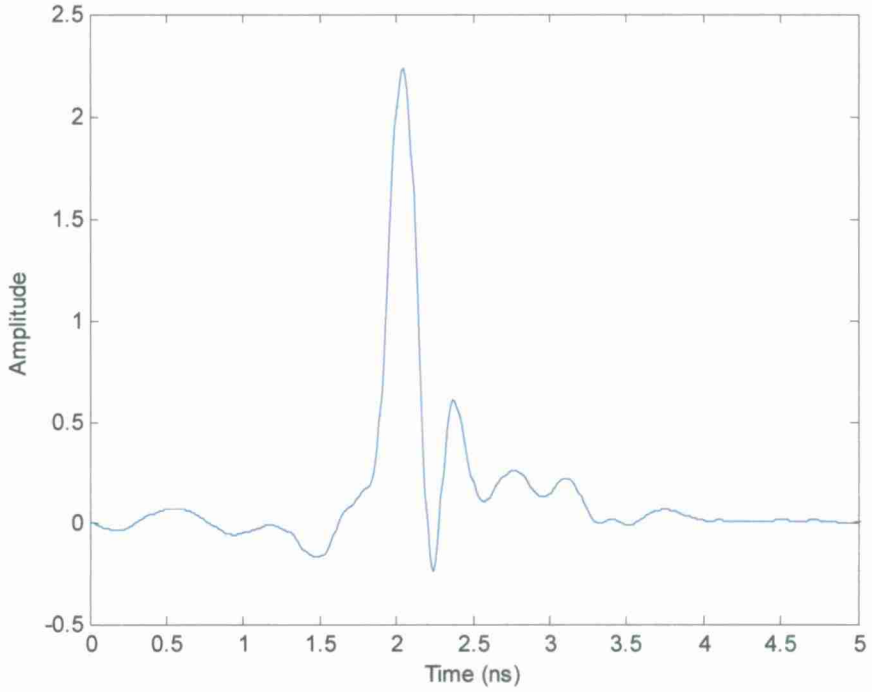


Figure 1. The wideband pulse used for imaging.

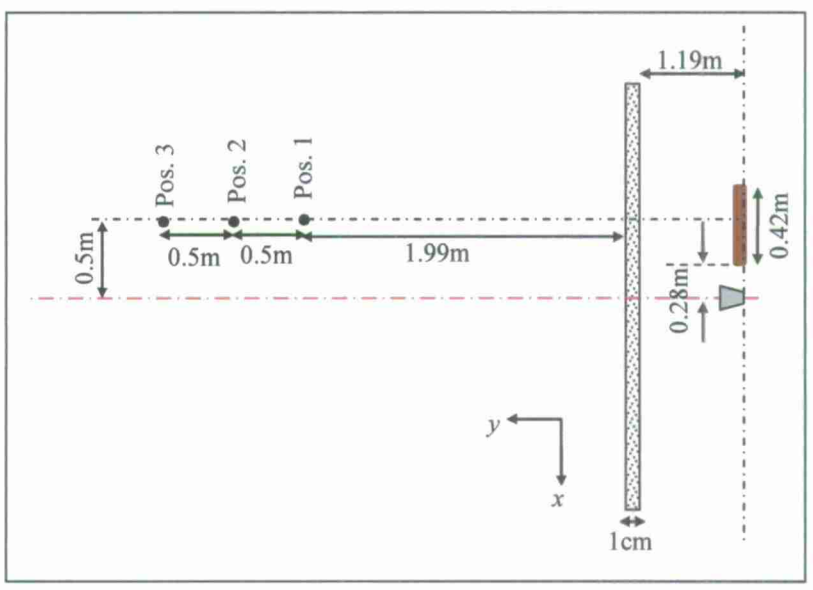


Fig. 2. Scene Layout for the target undergoing translational motion.

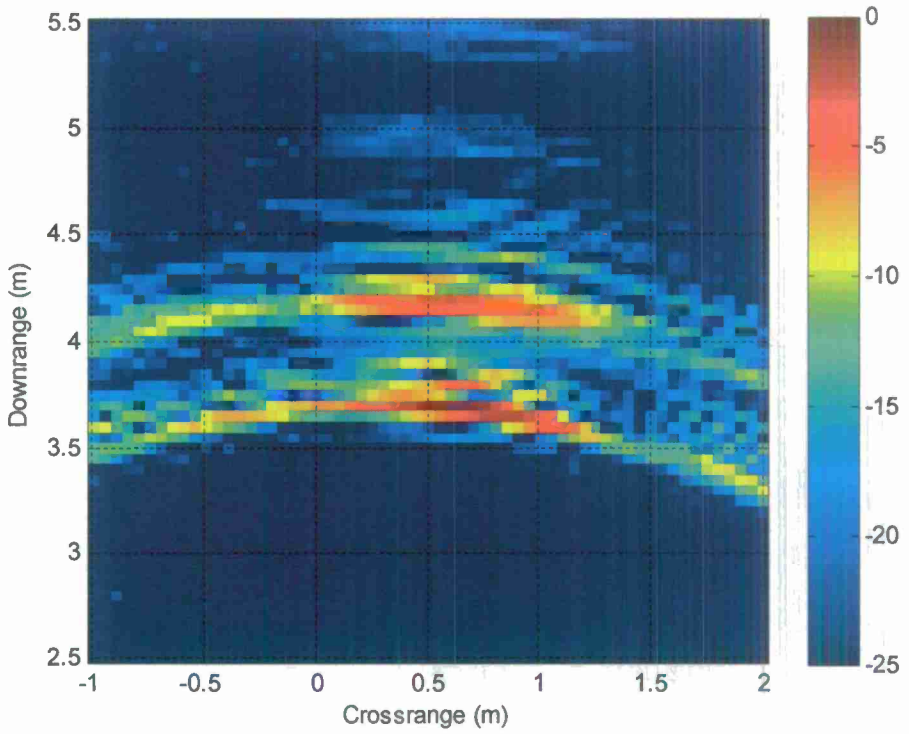


(a)

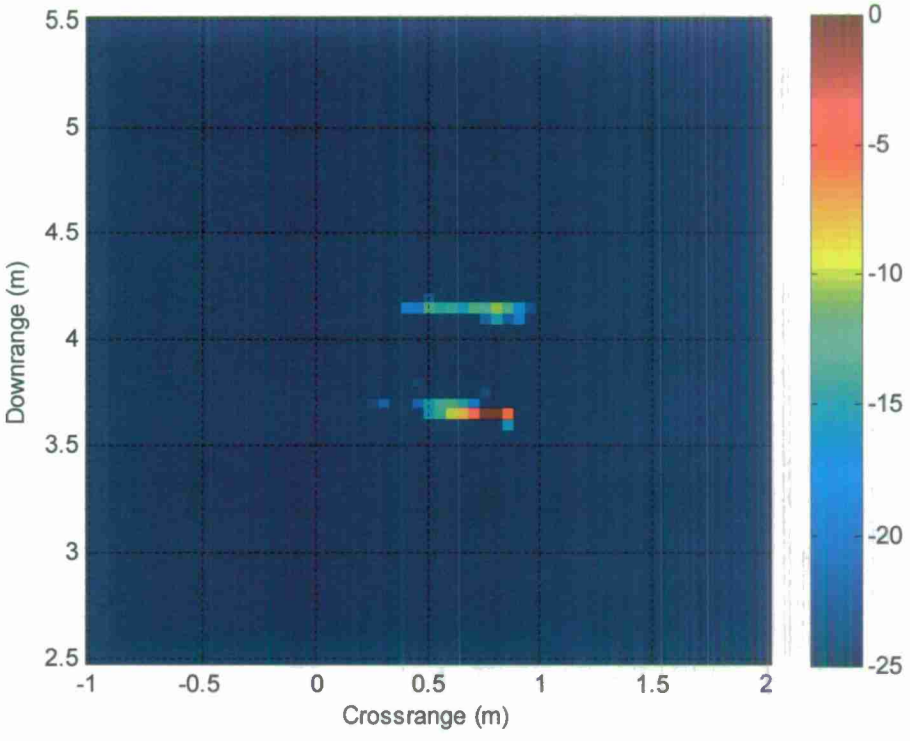


(b)

Figure 3. (a) Backprojection based CD image using the full dataset. (b) Sparsity-based CD image using 5% of the data volume, averaged over 100 trials.

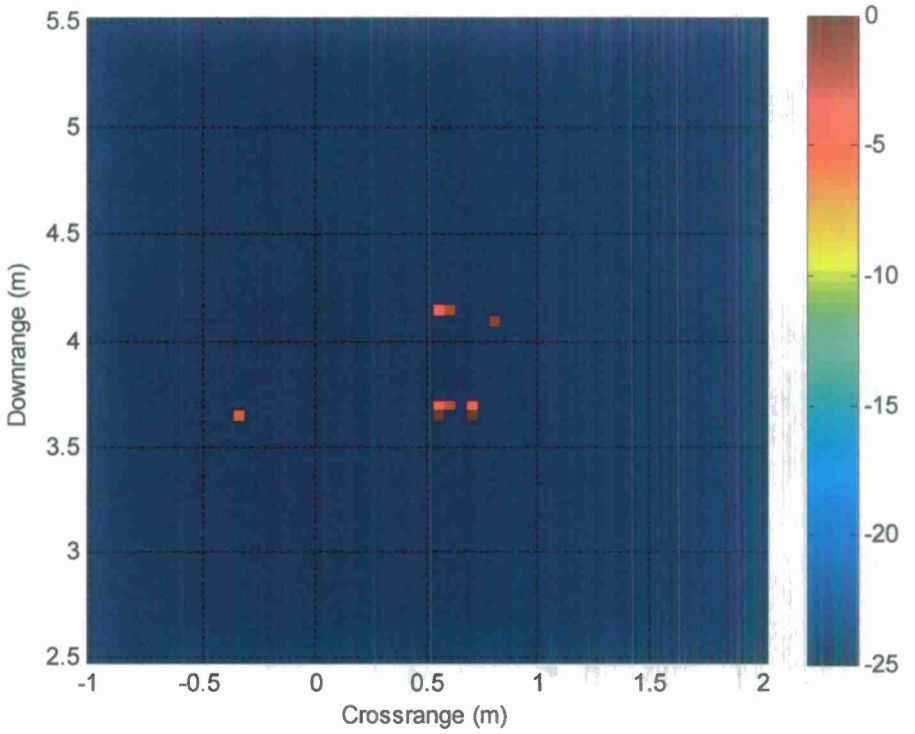


Figure 4. Sparsity-based CD image for one of the trials under translational motion.

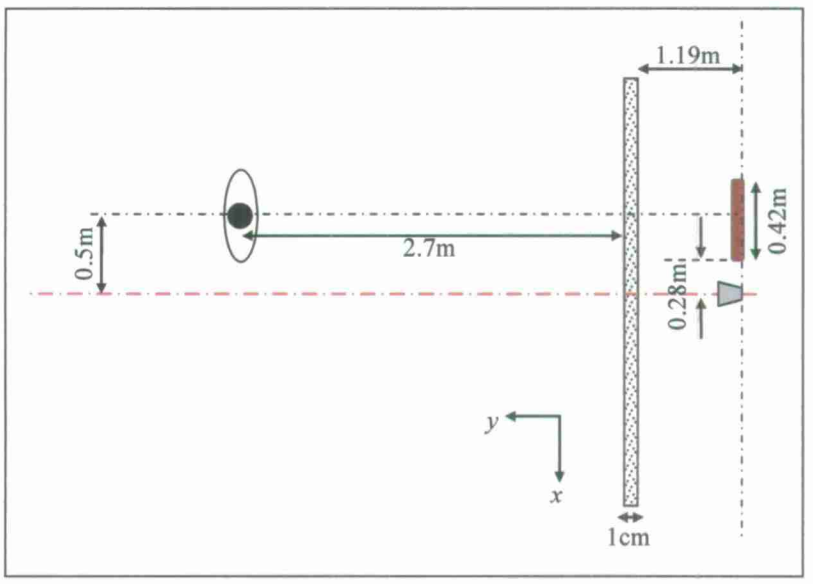


Figure 5. Scene layout for the target undergoing sudden short movement.

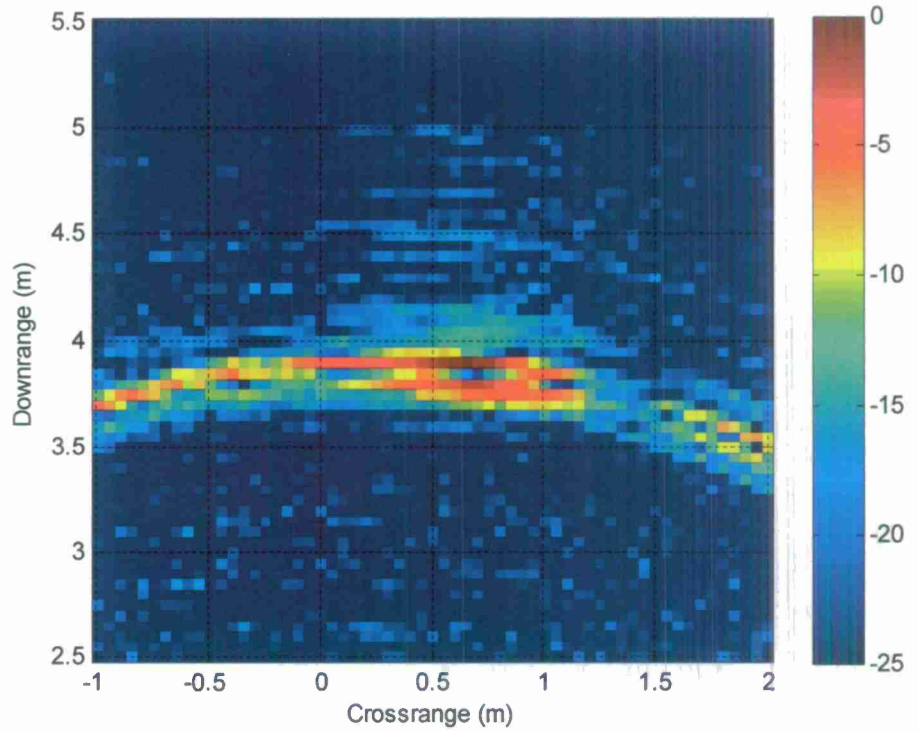


Figure 6. Backprojection based CD image using full data volume for the target undergoing short sudden movement.

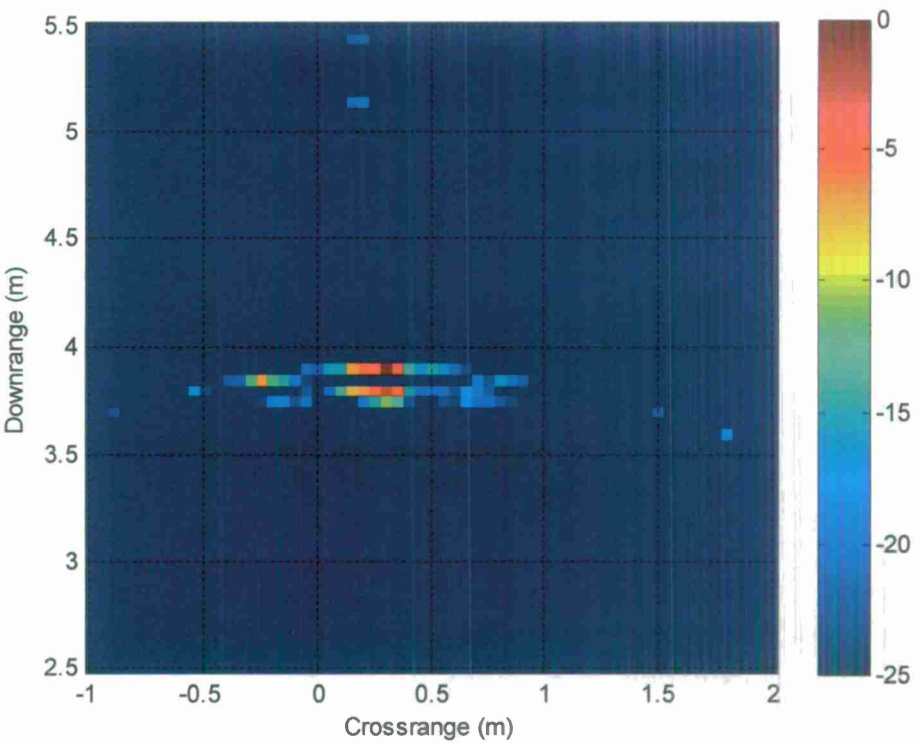


(a)

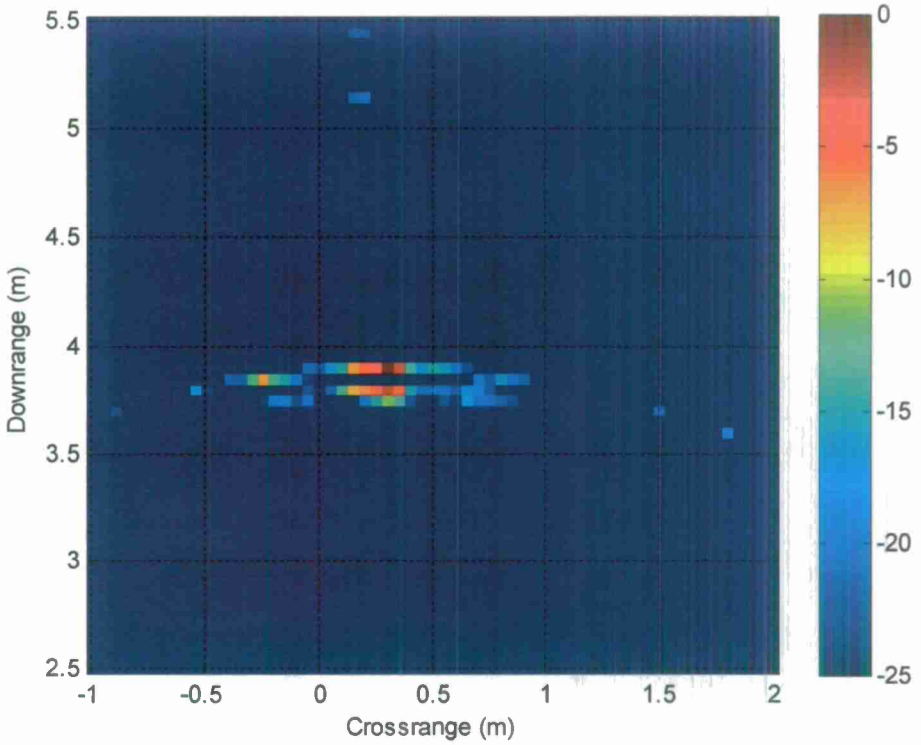


(b)

Figure 7. Sparsity-based composite images with 5% data volume for the sub-image combining approach in (a) eq. (25), and (b) eq. (26). The images are the averages of 100 reconstructions.

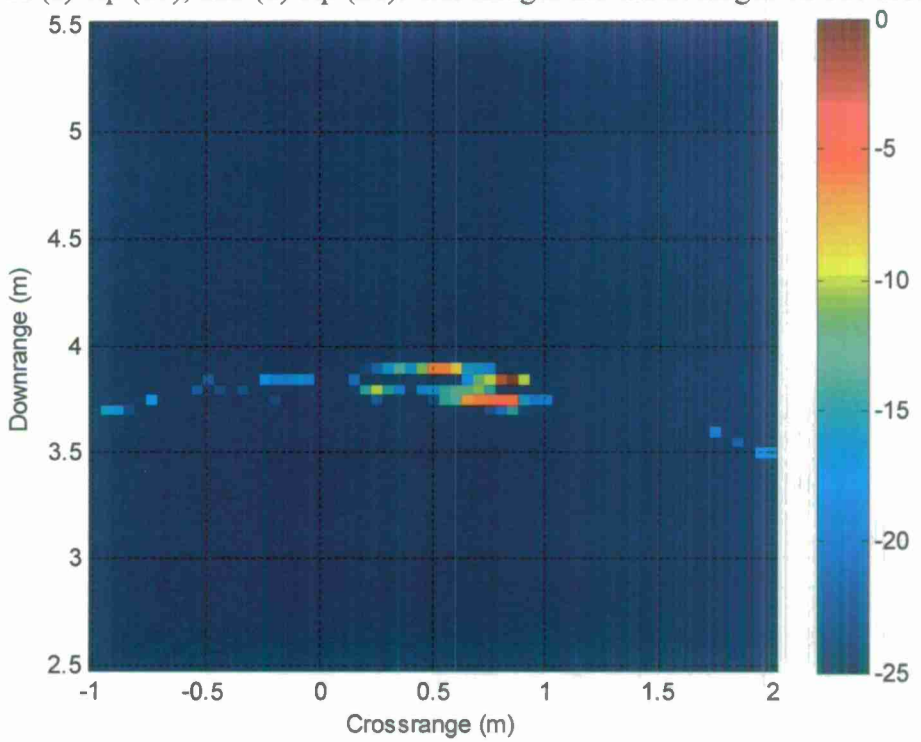


Figure 8. Sparsity-based image using 5% data volume without partitioning the receive array into sub-apertures.

# Chapter 2

## Joint Localization of Stationary and Moving Targets behind Walls using Sparse Scene Recovery

### 2.1. Introduction

With recent advances in both algorithm and component technologies, there are increasing demands on radar imaging systems to deliver high resolution images in both range and crossrange. This demand requires use of wideband signals and large array apertures, which in turn, leads to the collection and processing of large amounts of data along the spatial, temporal, and frequency dimensions. This trend is set to continue with the ever-present usage of radar sensors and wide deployment of radar sensor networks.

The generation of massive amounts of data presents a major challenge towards the objective of detecting and localizing moving and stationary targets of interest, such as humans and weapons, inside enclosed structures in an efficient and reliable manner in through-the-wall radar imaging (TWRI) and urban sensing applications [1]-[3]. The emerging field of compressive sensing (CS), which enables reconstruction of a sparse signal from far fewer nonadaptive measurements [4]-[5], provides an alternative for data reduction in radar imaging without compromising image quality [6]-[9]. For TWRI, these techniques offer efficient sensing operations that culminate in quick and reliable, actionable intelligence [10]-[15].

In TWRI, the presence of the front wall renders the target detection problem very difficult and challenging. The wall produces a strong radar return that not only tends to obscure the nearby inside targets, but also reduces the signal-to-clutter ratio (SCR) of the scene image. The low SCR, together with the fact that the wall is extended in crossrange and occupies several pixels in the image, renders the assumption of a sparse observed scene invalid. This has an adverse effect on the scene reconstruction performance when employing CS.

Different strategies have been devised for suppression of the wall clutter to enable target detection behind walls. Change detection was considered in [16]-[18], wherein the stationary background was removed by taking the difference of data observations over successive probing of the scene. Sparsity-driven imaging techniques were then applied to the difference signals to detect and localize the moving targets [12], [19]. Clutter cancellation filtering provides another option, which has been successfully applied as a preprocessing step in [20] and [21] for general multi-input multi-output (MIMO) radar and synthetic aperture radar (SAR) imaging applications. However, along with the wall clutter, both of these methods also suppress the returns from the stationary targets of interest in the scene, and as such, allow subsequent application of CS to recover only the moving targets. For wall-clutter mitigation in stationary scenes, several techniques have also been proposed in the last few years. For example, in an EM modeling based approach, the wall parameters are estimated from the radar returns, and then used to model and subtract the wall contributions from the received data [22]. This wall-dependent technique is effective under full data volume, but its performance is subject to wall estimation and modeling errors. Wall-independent methods, such as spatial filtering [23] and subspace projection [24], have been developed, and have been successfully applied to CS reconstruction [25]. However, these methods assume monostatic operation with the array located parallel to the front wall, and exploit the invariance of the wall return across the array under such a deployment for mitigating the wall return.

In this Chapter, we propose an alternate approach for jointly detecting and localizing stationary and moving targets behind walls, while simultaneously achieving a sizable reduction in the number of data measurements. We assume an ultra-wideband (UWB) pulse-Doppler imaging radar system with a physical multistatic aperture. We exploit the compact temporal

support of UWB signals to employ time gating [26]-[29], in lieu of the aforementioned clutter cancellation methods, for suppressing the wall returns. This enhances the SCR and maintains the sparsity of the scene, thereby permitting the application of CS techniques for streamlining data acquisition and scene reconstruction with few observations compared to conventional approaches.

The Chapter establishes an appropriate signal model that enables formulation of linear modeling with sensing matrices, so as to achieve reconstruction of the downrange-crossrange-velocity space via sparse recovery techniques. Supporting results based on real data collected in a laboratory environment are provided. It is shown that the sparsity-based scheme for joint localization of stationary and moving targets achieves a sizable reduction in the data volume without any degradation in the system performance.

The Chapter is organized as follows. In Section 2.2, we describe the UWB signal model for the multistatic imaging radar under the assumption of sequential use of the available transmitters. Conventional backprojection based downrange-crossrange-Doppler processing method is reviewed in Section 2.3. We present the sparsity-based stationary and moving target localization scheme in Section 2.4, highlighting the sensing matrix based linear modeling formulation. Section 2.5 provides the experiment results, depicting the performance of the sparsity-based localization scheme for the case of a few stationary and moving targets inside a room using reduced data volume. Conclusions are drawn in Section 2.6.

## 2.2. Ultra-Wideband Signal Model

In this section, we develop the signal model for ultra-wideband radar operation with $M$ transmitters and $N$ receivers. A sequential multiplexing of the transmitters with simultaneous reception at multiple receivers is assumed. Although this signaling approach demands more

acquisition time compared to the simultaneous transmitter operation, it is a viable option for TWRI operations. This is because a) More receivers than transmitters are deployed due to the important constraint of low cost, and b) The moving targets of interest have low velocities indoors. It is important to note that the sequential transmit operation is the salient feature of three known through-the-wall radar imaging systems; one is built by the Army Research Lab [16], the other by the Defense Research and Development Canada [30], and the third by MIT Lincoln Lab [31]. With the assumption of sequential multiplexing, a signal model can thus be developed based on single active transmitters.

Consider an $M$-element transmit array and an $N$-element receive array, both located along the $x$-axis at a standoff distance $y_{off}$ from a homogeneous wall, as shown in Fig. 1. Note that although the arrays are assumed to be parallel to the front wall for notational simplicity, this is not a requirement. Let $\mathbf{x}_{tm} = (x_{tm}, 0)$ and $\mathbf{x}_{rn} = (x_{rn}, 0)$ be the respective phase centers of the $m$th transmitter and the $n$th receiver. Let the transmit signal be expressed as

$$s(t) = a(t)\exp(j2\pi f_c t) \tag{1}$$

where $a(t)$ is the ultra-wideband baseband signal and $f_c$ is the carrier frequency, and let $T_r$ be the pulse repetition interval. Consider a coherent processing interval of $K$ pulses per transmitter and a single point target moving slowly away from the origin with constant horizontal and vertical velocity components $(v_{xp}, v_{yp})$, as depicted in Fig. 1. Let the target position be $\mathbf{x}_p = (x_p, y_p)$ at time $t = 0$. Assume that the timing interval for sequencing through the transmitters is short enough so that the target appears stationary during each data collection interval of length $MT_r$. This implies that the target position corresponding to the $k$th pulse is given by

$$\mathbf{x}_p(k) = (x_p + v_{xp} kMT_r, y_p + v_{yp} kMT_r) \tag{2}$$

The baseband target return measured by the *n*th receiver corresponding to the *k*th pulse emitted by the *m*th transmitter is given by

$$z_{mnk}^{p}(t) = \sigma_p a(t - kMT_r - mT_r - \tau_{mn,p}(k)) \exp(-j2\pi f_c \tau_{mn,p}(k)) \tag{3}$$

where $\sigma_p$ is the complex reflectivity of the target and $\tau_{mn,p}(k)$ is the propagation delay for the *k*th pulse to travel from the *m*th transmitter to the target at $\mathbf{x}_p(k)$, and back to the *n*th receiver. For through-the-wall propagation, $\tau_{mn,p}(k)$ comprises the components corresponding to traveling distances before, through, and after the wall [32]. In the presence of $P$ point targets, the received signal component corresponding to the targets will be a superposition of the individual target returns in (3) with $p = 0,1,\ldots,P-1$. Interactions between the targets and multipath returns are ignored in this model. Note that any stationary targets behind the wall are included in this model and would correspond to the motion parameter pair $(v_{xp}, v_{yp}) = (0, 0)$. Further note that the slowly moving targets are assumed to remain within the same range cell over the coherent processing interval.

On the other hand, as the wall is a specular reflector, the baseband wall return received at the *n*th receiver corresponding to the *k*th pulse emitted by the *m*th transmitter can be expressed as

$$z_{mnk}^{wall}(t) = \sigma_{wall} s(t - kMT_r - mT_r - \tau_{mn,wall}) \exp(-j2\pi f_c \tau_{mn,wall}) + B_{mnk}^{wall}(t) \tag{4}$$

where $\sigma_{wall}$ is the complex wall reflectivity, $\tau_{mn,wall}$ is the propagation delay from the *m*th transmitter to the wall and back to the *n*th receiver, and $B_{mnk}^{wall}(t)$ represents the wall

reverberations of decaying amplitudes resulting from multiple reflections within the wall (see Fig. 2). The propagation delay $\tau_{mn,wall}$ is given by [33]

$$\tau_{mn,wall} = \frac{\sqrt{(x_{tm} - x_{w,mn})^2 + y_{off}^2} + \sqrt{(x_{rn} - x_{w,mn})^2 + y_{off}^2}}{c} \tag{5}$$

where $c$ is the speed of light in free space, and

$$x_{w,mn} = \frac{x_{tm} + x_{rn}}{2}. \tag{6}$$

is the point of reflection on the wall corresponding to the $m$th transmitter and the $n$th receiver, as shown in Fig. 2. Note that, as the wall is stationary, the delay $\tau_{mn,wall}$ does not vary from one pulse to the next. Therefore, the expression in (4) assumes the same value for $k = 0,..., K-1$.

Combining (3) and (4), the total baseband signal received by the $n$th receiver, corresponding to the $k$th pulse with the $m$th transmitter active, is given by

$$z'_{mnk}(t) = z^{wall}_{mnk}(t) + \sum_{p=0}^{P-1} z^{p}_{mnk}(t) \tag{7}$$

The returns from behind-the-wall targets, both moving and stationary, are, in general, much weaker than the front wall reflections, resulting in a low SCR. Because of the UWB nature of the transmit signal, it is natural to remedy this situation by gating out the wall return in the time domain, thereby providing access to the sparse behind-the-wall scene of a few stationary and moving targets of interest. Therefore, the time-gated received signal contains only contributions from the $P$ targets behind the wall as well as any residuals of the wall not removed or fully mitigated by gating. In this Chapter, we assume that wall clutter is effectively suppressed by gating. Therefore, using (7), we obtain

$$z_{mnk}(t) = \sum_{p=0}^{P-1} z^{p}_{mnk}(t) \tag{8}$$

## 2.3. Backprojection Based Stationary and Moving Target Localization

Radar images are typically formed using the well-known backprojection algorithm [34]-[37]. High resolution imaging of stationary scenes for through-the-wall applications is considered in [38]-[41]. However, the presence of moving targets in the observed scene presents a problem for conventional backprojection. Unlike stationary targets, the moving targets are defocused and get smeared across the image. This makes it very difficult to detect and localize moving targets in the backprojected image [42]. Often, the approach to handling moving targets involves Doppler discrimination [43] in order to form a focused image of the moving targets. The simplest version is implemented as a Fast Fourier Transform (FFT) along the slow-time dimension of the raw data cube, followed by backprojection applied to the fast time vs. spatial data per Doppler bin, as illustrated in Fig. 3.

Consider the signal $\{z_{mnk}(t)\}_{k=0}^{K-1}$ received by the $n$th receiver with the $m$th transmitter active over the coherent processing interval, where $z_{mnk}(t)$ is given by (8). After application of the Fourier transform to $\{z_{mnk}(t)\}_{k=0}^{K-1}$ along slow time, let the resulting signal corresponding to the $l$th Doppler frequency bin be denoted by $z_{mn}^{l}(t)$. In order to generate the range vs. crossrange image corresponding to the $l$th Doppler bin, the signal $z_{mn}^{l}(t)$ corresponding to all $M$ transmitters and all $N$ receivers is processed as follows.

The region of interest is divided into a finite number of pixels, say $N_x \times N_y$, in crossrange and downrange. For the considered geometry of Fig. 1, the crossrange is represented by the $x$-axis and the $y$-axis is the downrange. The composite signal corresponding to the $q$th pixel, located at $\mathbf{x}_q = (x_q, y_q)$, can be obtained by applying focusing delays, and then summing the results [37],

$$z_q^l(t) = \sum_{m=0}^{M-1} \sum_{n=0}^{N-1} z_{mn}^l(t + \tau_{mn,q}) . \quad (9)$$

Note that the focusing delay $\tau_{mn,q}$ corresponds to the two-way signal propagation time between the $m$th transmitter, the $q$th pixel, and the $n$th receiver. If the target is indeed present at the $q$th pixel location, i.e., $\mathbf{x}_q = \mathbf{x}_p$, then the focusing delays align all the signals corresponding to the different transmitters and receivers, resulting in the signals being coherently combined. On the other hand, if there is no target at the $q$th pixel, the same focusing time delays will cause the various signals to stagger in time, thereby producing a reduced combined output.

The complex amplitude image value corresponding to the $q$th pixel is obtained from (9) as

$$I^l(\mathbf{x}_q) = z_q^l(t)\Big|_{t=0} . \quad (10)$$

The process described by (9) and (10) is performed for all $N_x \times N_y$ pixels to generate the complex image of the scene corresponding to the $l$th Doppler bin.

Note that it is possible to obtain the spatial and motion parameters of targets in the field of view even if some of the spatial-fast time-slow time measurements are missing. However, merely employing some of the transmit and receive elements, a few pulses, and/or part of the signal time duration, in the backprojection based scene reconstruction scheme degrades the image quality [44]. CS framework is, therefore, more suitable for pursuing reduction in data volume.

### 2.4. CS Based Stationary and Moving Target Localization

In this section, we develop the linear signal model with sensing matrices for application of CS and present the sparse reconstruction scheme for joint localization of stationary and moving targets inside enclosed structures.

### 2.4.1. Linear Model Formulation

With the observed scene divided into $N_x \times N_y$ pixels in crossrange and downrange, consider $N_{v_x}$ and $N_{v_y}$ discrete values of the expected horizontal and vertical velocities, respectively. Therefore, an image with $N_x \times N_y$ pixels in crossrange and downrange is associated with each considered horizontal and vertical velocity pair, resulting in a four-dimensional target space. Note that the considered velocities contain the (0, 0) velocity pair to include stationary targets.

Sampling the received signal $z_{mnk}(t)$ at times $\{t_i\}_{i=0}^{Q-1}$, we obtain a $Q \times 1$ vector $\mathbf{z}_{mnk}$. For the $l$th velocity pair $(v_{xl}, v_{yl})$, we vectorize the corresponding crossrange vs. downrange image into an $N_x N_y \times 1$ scene reflectivity vector $\boldsymbol{\sigma}(v_{xl}, v_{yl})$. The vector $\boldsymbol{\sigma}(v_{xl}, v_{yl})$ is a weighted indicator vector defining the scene reflectivity corresponding to the $l$th considered velocity pair, i.e., if there is a target at the spatial grid point $(x, y)$ with motion parameters $(v_{xl}, v_{yl})$, then the value of the corresponding element of $\boldsymbol{\sigma}(v_{xl}, v_{yl})$ should be nonzero; Otherwise, it is zero.

Using the developed signal model in (3) and (8), we obtain the linear system of equations,

$$\mathbf{z}_{nmk} = \boldsymbol{\Psi}_{nmk}(v_{xl}, v_{yl})\boldsymbol{\sigma}(v_{xl}, v_{yl}), \quad l = 0,1,\ldots,(N_{v_x} N_{v_y} - 1) \tag{11}$$

where the matrix $\boldsymbol{\Psi}_{mnk}(v_{xl}, v_{yl})$ is of dimension $Q \times N_x N_y$. The $q$th column of $\boldsymbol{\Psi}_{mnk}(v_{xl}, v_{yl})$ consists of the received signal corresponding to a target at pixel $\mathbf{x}_q$ with motion parameters $(v_{xl}, v_{yl})$ and the $i$th element of the $q$th column can be written as

$$\left[\boldsymbol{\Psi}_{mnk}(v_{xl}, v_{yl})\right]_{i,q} = s(t_i - kMT_r - mT_r - \tau_{mn,q}(k))\exp(-j2\pi f_c \tau_{mn,q}(k)) \tag{12}$$

where $\tau_{mn,q}(k)$ is the two-way signal traveling time, corresponding to $(v_{xl}, v_{yl})$, from the $m$th transmitter to the $q$th spatial grid point and back to the $n$th receiver for the $k$th pulse.

Stacking the received signal samples corresponding to $K$ pulses from all $MN$ transmitting and receiving element pairs, we obtain the $MNKQ \times 1$ measurement vector $\mathbf{z}$ as

$$\mathbf{z} = \mathbf{\Psi}(v_{xl}, v_{yl})\boldsymbol{\sigma}(v_{xl}, v_{yl}), \quad l = 0,1,\ldots,(N_{v_x} N_{v_y} - 1) \tag{13}$$

where

$$\mathbf{\Psi}(v_{xl}, v_{yl}) = \left[\mathbf{\Psi}^T_{000}(v_{xl}, v_{yl}), \ldots, \mathbf{\Psi}^T_{(M-1)(N-1)(K-1)}(v_{xl}, v_{yl})\right]^T. \tag{14}$$

Finally, forming the $MNKQ \times N_x N_y N_{v_x} N_{v_y}$ matrix $\mathbf{\Psi}$ as

$$\mathbf{\Psi} = \left[\mathbf{\Psi}(v_{x0}, v_{y0}), \ldots, \mathbf{\Psi}(v_{x(N_{vx}N_{vy}-1)}, v_{y(N_{vx}N_{vy}-1)})\right], \tag{15}$$

we obtain the linear matrix equation

$$\mathbf{z} = \mathbf{\Psi}\boldsymbol{\sigma} \tag{16}$$

with $\boldsymbol{\sigma}$ being the concatenation of target reflectivity vectors corresponding to every possible considered velocity combination.

### 2.4.2. CS Data Acquisition and Scene Reconstruction

The model described in (16) permits the scene reconstruction within the CS framework. We measure a $J < MNKQ$ dimensional vector of elements randomly chosen from **z.** The reduced set of measurements can be expressed as

$$\tilde{\mathbf{z}} = \mathbf{\Phi}\mathbf{\Psi}\boldsymbol{\sigma} \tag{17}$$

where $\mathbf{\Phi}$ is a $J \times MNKQ$ measurement matrix. For measurement reduction simultaneously along the spatial, slow time, and fast time dimensions, the specific structure of the matrix $\mathbf{\Phi}$ is given by

$$\mathbf{\Phi} = (\mathbf{\Phi}_1 \otimes \mathbf{I}_{Q_1 K_1 N_1}) \cdot (\mathbf{\Phi}_2 \otimes \mathbf{I}_{Q_1 K_1 M}) \cdot (\mathbf{\Phi}_3 \otimes \mathbf{I}_{Q_1 MN}) \cdot \mathrm{diag}(\mathbf{\Phi}_4^{(0)}, \ldots, \mathbf{\Phi}_4^{(MNK-1)}) \tag{18}$$

where '$\otimes$' denotes the Kronecker product, $\mathbf{I}_{(\cdot)}$ is an identity matrix with the subscript indicating its dimensions, and $M_1, N_1, K_1,$ and $Q_1$ denote the reduced number of transmit elements, receive elements, pulses, and fast time samples, respectively, with the total number of reduced measurements $J = M_1 N_1 K_1 Q_1$. The matrix $\mathbf{\Phi}_1$ is an $M_1 \times M$ matrix, $\mathbf{\Phi}_2$ is an $N_1 \times N$ matrix, $\mathbf{\Phi}_3$ is a $K_1 \times K$ matrix, and $\mathbf{\Phi}_4^{(i)}, i = 0,..., MNK-1$ is a $Q_1 \times Q$ matrix for determining the reduced number of transmitting elements, receiving elements, pulses and fast time samples, respectively. Each of the three matrices $\mathbf{\Phi}_1, \mathbf{\Phi}_2,$ and $\mathbf{\Phi}_3$ consists of randomly selected rows of an identity matrix. These choices of reduced matrix dimensions amount to selection of subsets of existing available degrees of freedom offered by the fully deployed imaging system. Any other matrix structure does not yield to any hardware simplicity or saving in acquisition time. On the other hand, three different choices are available for compressive acquisition of each pulse in fast time [45]. That is, the matrix $\mathbf{\Phi}_4^{(i)}, i = 0,\ldots, MNK-1,$ can be 1) a Gaussian random matrix with entries drawn from $\mathbf{N}(0,1)$, 2) a random matrix with entries equal to $\pm 1$ with probability ½, or 3) a matrix consisting of randomly selected rows of an identity matrix. The three options provide tradeoff between the imaging performance and ease of hardware implementation, as discussed in detail in [45]. A possible receiver hardware implementation for the first two types of random matrices is depicted in Fig. 4 using the $i_n$ th receive element with the $i_m$ th transmit element active, where $i_n \in \{0,1,..., N-1\}$ and $i_m \in \{0,1,..., M-1\}$ are the indices of the randomly selected reduced set of receivers and transmitters. The reduced number of pulses is assumed to be transmitted in a random fashion, with the receiver synchronized to the transmitter. Further assume $T_0, T_1,..., T_{K_1-1}$ to be the time period between consecutive transmissions in the sequence of

randomly selected $K_1$ pulses, as shown in Fig. 4. The switch implements the time gating for wall return removal and the time-gated signals are input to the subsequent random fast time measurement system. Each pulse is first multiplied by each column of the fast time measurement matrix and the product is then integrated. Both of these operations can be implemented by microwave mixers and low-pass filters [45]. The subsequent sampling operation in the system can, thus, furnish 'clean' data without the wall returns at a reduced volume.

Given the reduced measurement vector $\tilde{\mathbf{z}}$ in (17), we can recover $\boldsymbol{\sigma}$ by solving the following equation,

$$\hat{\boldsymbol{\sigma}} = \arg\min_{\boldsymbol{\sigma}} \|\boldsymbol{\sigma}\|_1 \text{ subject to } \tilde{\mathbf{z}} \approx \boldsymbol{\Phi}\boldsymbol{\Psi}\boldsymbol{\sigma} \tag{19}$$

The problem in (19) can be solved using convex relaxation, greedy pursuit, or combinatorial algorithms [46]-[48]. In this work, we use OMP for the CS based reconstruction [49]. We note that the reconstructed vector can be rearranged into $N_{v_x} N_{v_y}$ matrices of dimensions $N_x \times N_y$ in order to depict the estimated target reflectivity for different vertical and horizontal velocity combinations. The stationary targets will be localized for the (0,0) velocity pair.

Further note that if the wall clutter is not totally mitigated and the wall residuals are comparable in strength to the target returns, then the image will contain artifacts resulting from reconstruction of the wall residuals. Also, OMP may require relatively more iterations to recover the targets in this case.

### 2.5. Experimental Results

An ultra-wideband pulsed radar system was used to perform real data measurements of a through-the-wall scene of stationary and moving targets in the Radar Imaging Lab at Villanova University. The radar employs a 0.7 ns Gaussian pulse for scene interrogation. The pulse is up-converted to 3 GHz for transmission and down-converted to baseband through in-phase and

quadrature demodulation on reception. The operational bandwidth of the radar system extends from 1.5 to 4.5 GHz. The peak transmit power is 25 dBm. Transmission is through a single horn antenna, model BAE-H1479, with an operational bandwidth from 1 to 12.4 GHz, which is mounted on a tripod. An 8-element uniform line array of Vivaldi elements with an inter-element spacing of 0.06 m, is used as the receiver and is placed to the right of the transmit antenna. The center-to-center separation between the transmitter and the leftmost receive antenna is 0.3 m, as shown in Fig. 5. A 3.65 m × 2.6 m wall segment was constructed utilizing 1 cm thick cement board on a 2-by-4 wood stud frame. The transmit antenna and the receive array were at a standoff distance of 1.19 m from the wall. The radar has a pulse repetition frequency (PRF) of 10 MHz. Despite the high PRF, the system refresh rate is 100Hz. This is because a) Equivalent time sampling is used [50], and b) Instead of simultaneous reception, the receive array elements are accessed sequentially through a multiplexer.

The origin of the coordinate system was chosen to be at the center of the receive array. The scene behind the wall consisted of one stationary target and one moving target, as shown in Fig. 5. A metal sphere of 0.3 m diameter, placed on a 1 m high Styrofoam pedestal, was used as the stationary target. The pedestal was located 1.25 m behind the wall, centered at (0.49 m, 2.45 m). A person walked towards the front wall at a speed of 0.7 m/s approximately along a straight line path, which is located 0.2 m to the right of the transmitter. The back and the right side wall in the region behind the front wall were covered with RF absorbing material, whereas the 8 in thick concrete side wall on the left and the floor were uncovered. A coherent processing interval of 15 pulses was selected.

The image region is chosen to be 4 m × 6 m, centered at (-0.31 m, 3 m), and divided into 41 × 36 pixels in crossrange and downrange. As the human moves directly towards the radar, we

only consider varying vertical velocity from -1.4 m/s to 0 m/s, with a step size of 0.7 m/s, resulting in three velocity pixels. In the following, we present the scene reconstruction results both with and without time gating of the front wall return. For the CS based reconstruction, the random measurement matrices $\mathbf{\Phi}_4^{(i)}$ are chosen to be the same for each pulse.

### 2.5.1. Scene Reconstruction without Time Gating

The space-slow time-fast time response of the scene consists of 8 × 15 × 2872 measurements. Figure 6 shows the backprojection-based images of the scene using all 8 × 15 × 2872 data points. In these and all subsequent images, we plot the image intensity on a 45 dB scale, with the intensity normalized to the maximum over the total target space. As discussed in Section III, we first performed Doppler filtering through an FFT operation along slow time, and then chose the Doppler bins corresponding to 0 and 14 Hz from the resulting space-fast time-Doppler data cube to form the respective images corresponding to the stationary target (see Fig. 6(a)) and the target moving at a velocity of -0.7 m/s (see Fig. 6(b)). The true positions of both targets are indicated by white ovals. We observe from Fig. 6(a) that the stationary target is barely detected due to the strong wall return. Although the moving target is correctly localized in Fig. 6(b), spectral leakage due to the high sidelobe energy from the much stronger stationary wall contaminates the moving target image.

For the CS based reconstruction, only 33.3% of the 15 pulses and 13.9% of the fast-time samples are randomly selected for each of the 8 receive elements, resulting in 8 × 5 × 400 space-slow time-fast time measured data. This is equivalent to 4.6% of the total data volume. More specifically, the 400 fast time samples at each receive element were obtained with a Gaussian random matrix, whose elements are drawn from $\mathbf{N}(0,1)$. The reduction in the slow time data was achieved with a matrix whose entries were selected randomly from rows of an identity matrix.

We reconstructed the target space using the proposed CS scheme with 4.6% data volume fifty times. For each trial, a different overall random measurement matrix was used to generate the reduced set of measurements, followed by sparse scene reconstruction with the number of OMP iterations set to 50. Figure 7 depicts the CS based result, averaged over fifty trials, corresponding to the three velocity bins. The higher the intensity of a pixel in this figure, the greater is the number of times that pixel was populated during the 50 reconstruction trials. We observe from Figs. 7(a) and 7(b) that both the stationary sphere and the moving person cannot be localized. The reason behind this failure is two-fold: 1) The front wall is a strong extended target and as such, most of the degrees of freedom of the reconstruction process are used up for the wall, and 2) The low SCR, due to the much weaker returns from the moving and stationary targets compared to the front wall reflections, causes the targets to be not reconstructed with the residual degrees of freedom of the OMP. These results confirm that the performance of the sparse reconstruction scheme is hindered by the presence of the front wall.

### 2.5.2. Scene Reconstruction after Time Gating

After removal of the front wall return from the received signals through time gating, the space-slow time-fast time data includes $8 \times 15 \times 2048$ measurements. The full time-gated data was used for scene reconstruction with the backprojection based approach. The resulting images are depicted in Figs. 8(a) and 8(b), for the 0 Hz and 14 Hz Doppler bins, respectively. Clearly, in the absence of the wall, the algorithm has successfully detected and localized both stationary and moving targets.

Figure 9 provides the corresponding result of OMP reconstruction, averaged over fifty trials. In each trial, we used all eight receivers, randomly selected 5 pulses (33.3% of 15) and chose 400 Gaussian random measurements (19.5% of 2048) in fast time, which amounts to using 6.5% of

the total data volume. The number of OMP iterations was set to 4. Figures 9(a), 9(b), and 9(c) are the respective images corresponding to the 0 m/s, -0.7 m/s, and -1.4 m/s velocities. It is apparent that with the wall removed, both the stationary and moving targets have been correctly localized even with the reduced set of measurements.

### 2.5.3. Computational Complexity

For a scene of sparsity $L$, the computational complexity of OMP is $O(N_x N_y N_{v_x} N_{v_y} M_1 N_1 K_1 Q_1 L)$ [51]. On the other hand, conventional backprojection employing the full dataset has a complexity of $O((N_x N_y N_{v_x} N_{v_y} + QU\log_2 QU)MNK)$, where $U$ is the upsampling ratio for fast-time interpolation [52]. We computed the complexity associated with backprojection and CS-based method employing OMP for the examples in Sections V.A and V.B. The upsampling ratio was selected to be 20 in both cases, while the sparsity was taken to be 4 and 50, respectively, for CS reconstruction with and without time-gating. The results are provided in Table I. For the considered parameters, backprojection and OMP have comparable computational complexity when time-gating is employed, while backprojection is an order of magnitude less computationally intensive than OMP when the wall return is not gated out.

## 2.6. Conclusion

We presented a compressive sensing based data acquisition and image reconstruction technique for joint localization of stationary and moving targets in through-the-wall radar imaging and urban sensing applications. We suppressed the front wall returns through time gating, which was made possible by the short temporal support characteristic of the UWB transmit waveform. The SCR enhancement as a result of time gating permits the application of CS techniques for scene reconstruction with few observations. We established an appropriate signal model that enabled formulation of linear modeling with sensing matrices for the problem of sparsity based

reconstruction of the downrange-crossrange-velocity space. Results based on real data experiments demonstrated that joint localization of stationary and moving targets can be achieved via sparse regularization using a reduced set of measurements without any degradation in system performance.

## 2.7. References


[1] M. G. Amin (Ed.), *Through-the-Wall Radar Imaging*, CRC Press, Boca Raton, FL, 2010.

[2] M. G. Amin (Ed.), "Special issue on Advances in Indoor Radar Imaging," *J. Franklin Inst.*, vol. 345, no. 6, pp. 556–722, Sept. 2008.

[3] M. G. Amin and K. Sarabandi (Eds.), "Special issue on Remote Sensing of Building Interior," *IEEE Trans. Geosci. Remote Sens.*, vol. 47, no. 5, pp. 1270–1420, 2009.

[4] E. Candes, J. Romberg, and T. Tao, "Stable signal recovery from incomplete and inaccurate measurements," *Communications in Pure and Applied Math.*, vol. 59, pp. 1207-1223, 2006.

[5] E. J. Candes and M. B. Wakin, "An introduction to compressed sampling," *IEEE Signal Process. Mag.*, vol. 25, no. 2, pp. 21-30, 2008.

[6] R. Baraniuk and P. Steeghs, "Compressive radar imaging," in *Proc. IEEE Radar Conf.*, Waltham, MA, April 2007, pp. 128-133.

[7] M. C. Shastry, R. M. Narayanan, and M. Rangaswamy, "Compressive radar imaging using white stochastic waveforms," in *Proc. Intl. Waveform Diversity and Design Conf.*, Niagara Falls, Canada, pp. 90-94, Aug. 2010.

[8] L. C. Potter, E. Ertin, J. T. Parker, and M. Cetin, "Sparsity and compressed sensing in radar imaging," *Proc. of the IEEE,* vol. 98, no. 6, pp. 1006-1020, 2010.

[9] F. Ahmad (Ed.), *Compressive Sensing*, Proc. SPIE, vol. 8365, SPIE, Bellingham, WA, 2012.

[10] Y.S. Yoon and M. G. Amin, "Compressed sensing technique for high-resolution radar imaging," in *Proc. SPIE*, vol. 6968, pp. 69681A–1–69681A–10, 2008.

[11] Q. Huang, L. Qu, B. Wu, and G. Fang, "UWB through-wall imaging based on compressive sensing," *IEEE Trans. Geosci. Remote Sens.*, vol. 48, no. 3, pp. 1408-1415, 2010.

[12] M. G. Amin, F. Ahmad, and W. Zhang, "A compressive sensing approach to moving target indication for urban sensing," in *Proc. IEEE Radar Conf.*, Kansas City, MO, 2011.

[13]M. Leigsnering, C. Debes, and A. M. Zoubir, "Compressive sensing in through-the-wall radar imaging," in *Proc. IEEE Int. Conf. Acoustics, Speech and Signal Process.*, Prague, Czech Republic, 2011, pp. 4008–4011.

[14] F. Ahmad and M. G. Amin, "Partially Sparse Reconstruction of Behind-the-Wall Scenes," in *Proc. SPIE, Compressive Sensing Conf.*, Baltimore, MD, vol. 8365, Apr. 2012.

[15] R. Solimene, F. Ahmad, and F. Soldovieri, "A novel CS-TSVD strategy to perform data reduction in linear inverse scattering problems," *IEEE Geosci. Remote Sens. Lett.*, vol. 9, no. 5, pp. 881–885, 2012.

[16] A. Martone, K. Ranney, and R. Innocenti, "Through-the-wall detection of slow-moving personnel," in *Proc. SPIE*, vol. 7308, pp. 73080Q1-73080Q12, 2009.

[17] X. P. Masbernat, M. G. Amin, F. Ahmad, and C. Ioana, "An MIMO-MTI approach for through-the-wall radar imaging applications," in *Proc. 5th Int. Waveform Diversity and Design Conf.*, 2010.

[18] M. G. Amin and F. Ahmad, "Change detection analysis of humans moving behind walls," *IEEE Trans. Aerospace and Electronic Systems*, vol. 49, no. 1, January 2013.

[19] F. Ahmad and M. G. Amin, "Through-the-wall human motion indication using sparsity-driven change detection," *IEEE Trans. Geosci. Remote Sens.*, vol. 50, no. 12, 2012.

[20] Y. Yu and A. P. Petropulu, "A study on power allocation for widely separated CS-based MIMO radar," in *Proc. SPIE, Compressive Sensing Conf.*, Baltimore, MD, vol. 8365, Apr. 2012.

[21] A. S. Khawaja and J. Ma, "Applications of compressed sensing for SAR moving-target velocity estimation and image compression," *IEEE Trans. Instrumentation and Measurement*, vol. 60, no. 8, pp. 2848-2860, 2011.

[22] M. Dehmollaian and K. Sarabandi, "Refocusing through building walls using synthetic aperture radar," *IEEE Trans. Geosci. Remote Sens.*, vol. 46, no. 6, pp. 1589–1599, 2008.

[23] Y-S. Yoon and M. G. Amin, "Spatial filtering for wall-clutter mitigation in through-the-wall radar imaging," *IEEE Trans. Geosci. Remote Sens.*, vol. 47, no. 9, pp. 3192–3208, 2009.

[24] F. Tivive, M. Amin, and A. Bouzerdoum, "Wall clutter mitigation based on eigen-analysis in through-the-wall radar imaging," in *Proc. IEEE Workshop on DSP*, 2011.

[25]E. Lagunas, E., M. Amin, F. Ahmad, F. and M. Najar, "Joint wall mitigation and compressive sensing for indoor image reconstruction," *IEEE Trans. Geosci. Remote Sens.*, vol. 50, no. 12, 2012.

[26] J. D. Park and W. J. Kim, "An efficient method of eliminating the range ambiguity for a low-cost FMCW radar using VCO tuning characteristics," *IEEE Trans. Microw. Theory Techn.*, vol. 54, no. 10, pp. 3623-3629, Oct. 2006.

[27] R. Solimene, A. D'Alterio, and F. Soldovieri, "Half-space estimation by time gating based strategy," in *Proc. 13th Int. Conf. Ground Penetrating Radar*, 21-25, Jun. 2010, pp.1-5.

[28] Y. Wang and A. E. Fathy, "Advanced system level simulation platform for three-dimensional UWB through-wall imaging SAR using time-domain approach," *IEEE Trans. Geosci. Remote Sens.*, vol. 50, no. 5, pp. 1986-2000, May 2012.

[29] H. Von Aschen, F. Gumbmann, and L.-P. Schmidt, "High resolution permittivity reconstruction of one dimensional stratified dielectric media from broadband measurement data in the W-band," in *Proc. 2011 European Radar Conf.*, 12-14, Oct. 2011, pp.45-48.

[30] P. Sévigny et al., "Concept of operation and preliminary experimental results of the DRDC through-wall SAR system," in *Proc. SPIE*, vol. 7669, pp. 766907-1–766907-11, 2010.

[31] T. S. Ralston, G. L. Charvat, and J. E. Peabody, "Real-time through-wall imaging using an ultrawideband multiple-input multiple-output (MIMO) phased array radar system," in *Proc. IEEE Intl. Symp. Phased Array Systems and Technology*, pp. 551-558, 2010.

[32] M. G. Amin and F. Ahmad, "Wideband synthetic aperture beamforming for through-the-wall imaging," *IEEE Signal Process. Mag.*, vol. 25, no. 4, pp. 110-113, July 2008.

[33] F. Ahmad, M. G. Amin, and J. Qian, "Through-the-wall moving target detection and localization using sparse regularization," in *Proc. SPIE, Compressive Sensing Conf.*, Baltimore, MD, vol. 8365, Apr. 2012.

[34] M. Soumekh, *Synthetic Aperture Radar Signal Processing with Matlab Algorithms*, John Wiley and Sons, New York, NY, 1999.

[35] V. T. Vu, T. K. Sjogren, and M. I. Pettersson, "Fast backprojection algorithm for UWB bistatic SAR," in *Proc. IEEE Radar Conf.*, Kansas City, MO, 2011, pp. 431-434.

[36] R. L. Moses and J. N. Ash, "An autoregressive formulation for SAR backprojection imaging," *IEEE Trans. Aerosp. Electronic Syst.*, vol. 47, no. 4, pp. 2860-2873, Oct. 2011.

[37] F. Ahmad, G. J. Frazer, S. A. Kassam, and M. G. Amin, "Design and implementation of near-field, wideband synthetic aperture beamformers," *IEEE Trans. Aerosp. Electronic Syst.*, vol. 40, no. 1, pp. 206-220, Jan. 2004.

[38] F. Ahmad, M. G. Amin, and S. A. Kassam, "A beamforming approach to stepped-frequency synthetic aperture through-the-wall radar imaging," in *Proc. 1st IEEE Int. Workshop on Computational Advances in Multi-sensor Adaptive Process.*, Puerto Vallarta, Mexico, Dec. 2005.

[39] F. Ahmad and M. G. Amin, "High-resolution imaging using Capon beamformers for urban sensing applications," in *Proc. IEEE Int. Conf. on Acoustics, Speech, and Signal Process.*, Honolulu, HI, Apr. 2007.

[40] Y-S. Yoon and M. G. Amin, "High-resolution through-the-wall radar imaging using beamspace MUSIC," *IEEE Trans. on Antennas and Propagation*, vol. 56, no. 6, pp. 1763-1774, Jun. 2008.

[41] Y-S. Yoon, M. G. Amin, and F. Ahmad, "MVDR beamforming for through-the-wall radar imaging," *IEEE Trans. Aerosp. Electronic Syst.*, vol. 47, no. 1, pp. 347-366, January 2011.

[42] M. Ferrara, J. Jackson, and M. Stuff, "Three-dimensional sparse-aperture moving-target imaging," in *Proc. SPIE*, vol. 6970, 2008.

[43] M. Skolnik (Ed.), *Introduction to Radar Systems*, 3rd Edition, McGraw Hill, New York, NY, 2001.

[44] L. He, S. A. Kassam, F. Ahmad, and M. G. Amin, "Sparse multi-frequency waveform design for wideband imaging," in *Principles of Waveform Diversity and Design*, M. Wicks, E. Mokole, S. Blunt, R. Schneible, V. Amuso (Eds.), SciTech Publishing, 2010, pp. 922-938.

[45] A. C. Gurbuz, J. H. McClellan, and W. R. Scott, Jr., "Compressive sensing for subsurface imaging using ground penetrating radar," *Signal Process.*, vol. 89, no. 10, pp. 1959-1972, 2009.

[46] S. Boyd and L. Vandenberghe, *Convex Optimization*, Cambridge University Press, 2004.

[47] S. S. Chen, D. L. Donoho, and M. A. Saunders, "Atomic decomposition by basis pursuit," *SIAM J. Scientific Computing*, vol. 20, no. 1, pp. 33–61, 1999.

[48] J. A. Tropp, "Greed is good: Algorithmic results for sparse approximation," *IEEE Trans. Inf. Theory*, vol. 50, no. 10, pp. 2231–2242, 2004.

[49] J. A. Tropp and A. C. Gilbert, "Signal recovery from random measurements via orthogonal matching pursuit," *IEEE Trans. Inf. Theory*, vol. 53, no. 12, pp. 4655–4666, 2007.

[50] Y. Yang and A. Fathy, "Development and implementation of a real-time see-through-wall radar system based on FPGA," *IEEE Trans. Geosci. Remote Sens.*, vol. 47, no. 5, pp. 1270-1280, 2009.

[51] W. U. Bajwa and A. Pezeshki, "Finite frames for sparse signal processing," in *Finite Frames*, P. Casazza and G. Kutyniok, (Eds.), Cambridge, MA: Birkhäuser Boston, 2012, pp. 303-335.

[52] L. Rosenberg and D. Gray, "Multichannel SAR imaging with backprojection," in *Proc. Intelligent Sensors, Sensor Networks and Information Processing Conf.*, 14-17 Dec. 2004, pp. 265- 270.

Table I. Algorithm Complexity

| **Example** | **Backprojection** | **OMP** |
|---|---|---|
| Without Time Gating | $1.095\times10^{8}$ | $3.54\times10^{9}$ |
| With Time Gating | $7.584\times10^{7}$ | $2.83\times10^{8}$ |

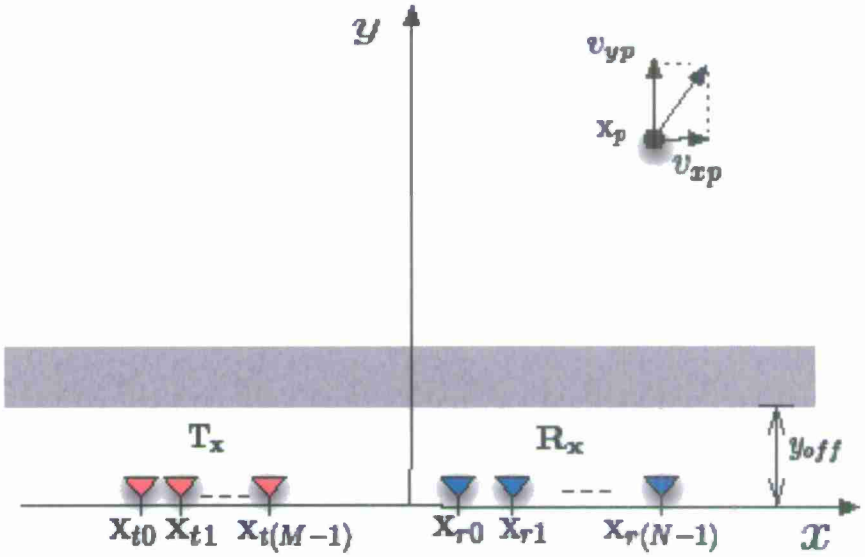


Fig.1. Geometry on transmit and receive.

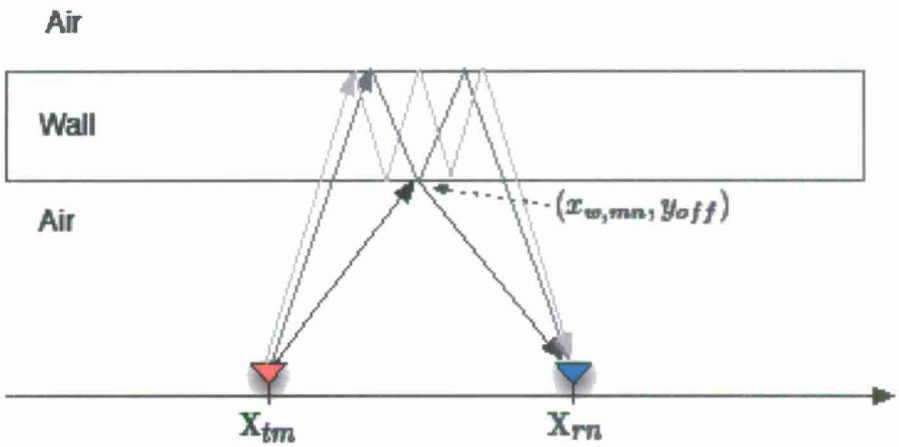


Fig. 2. Wall reverberations.

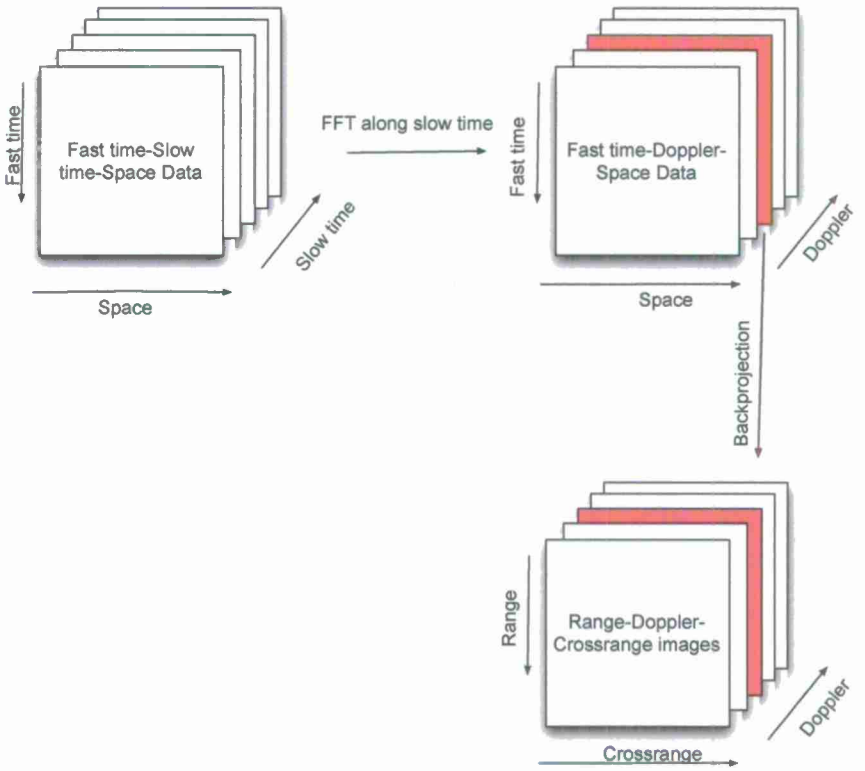


Fig. 3. Flowchart of conventional backprojection based imaging scheme.

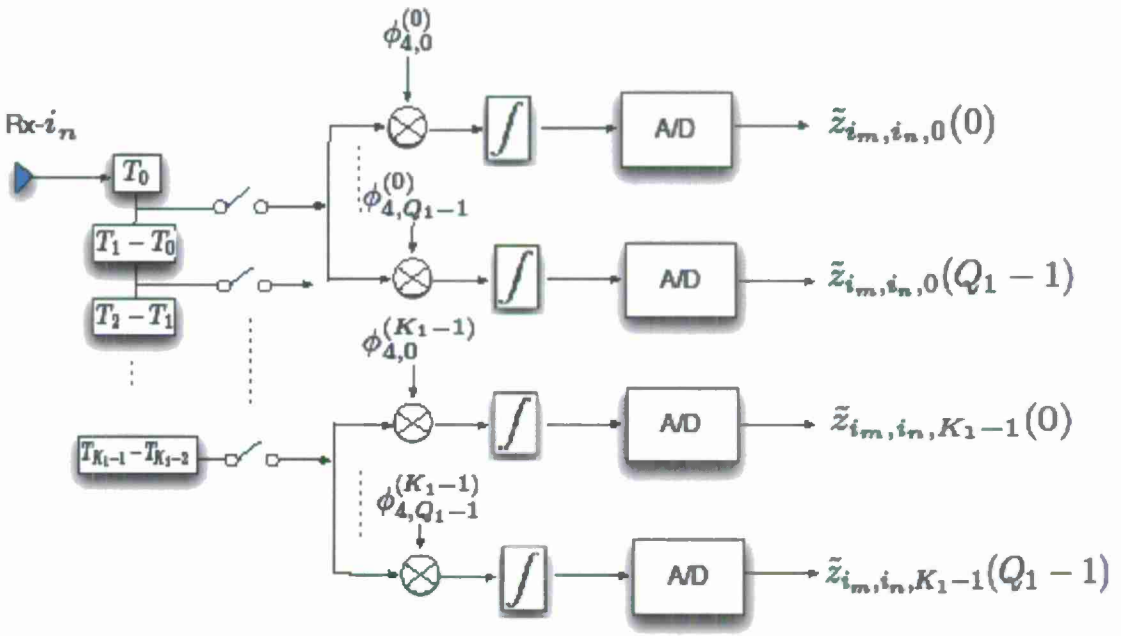


Fig. 4. Receiver Implementation for compressive ultra-wideband through-the-wall radar.

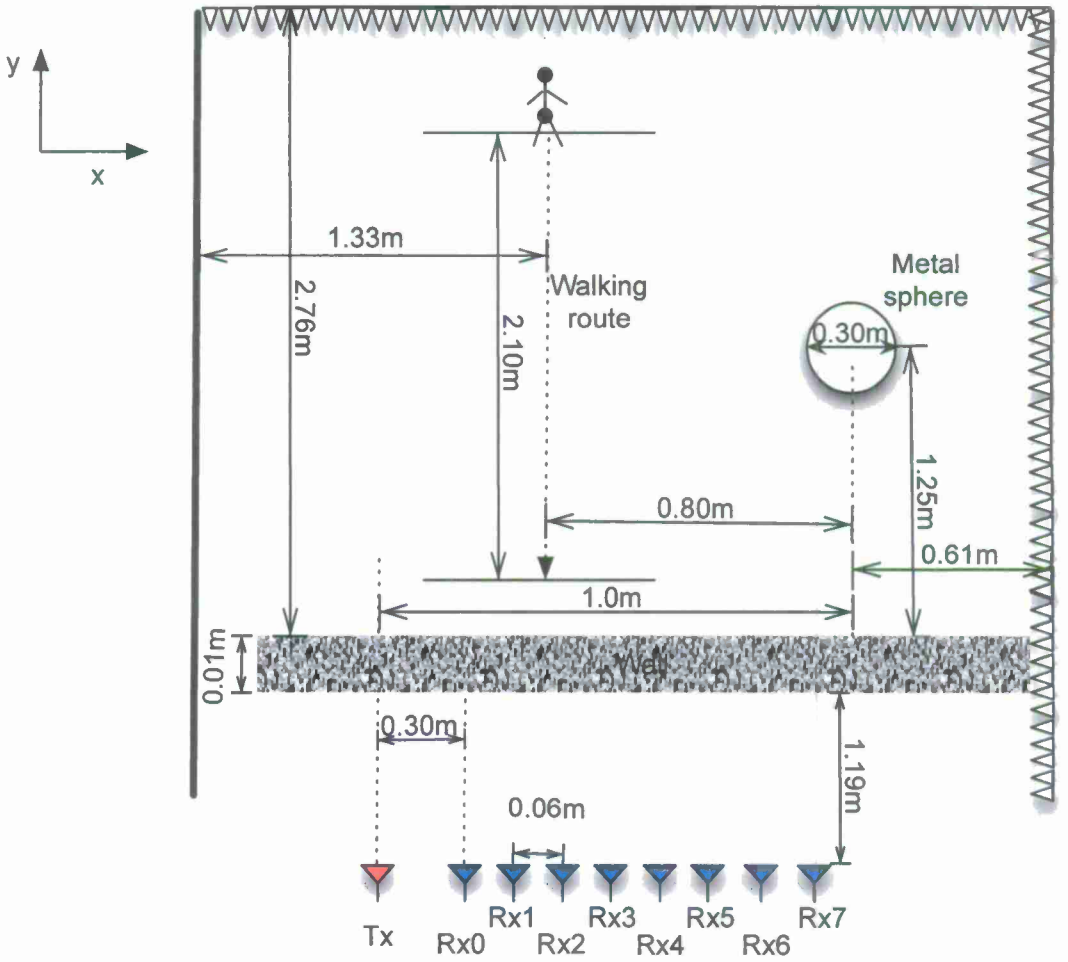


Fig. 5. The configuration of the experiment.

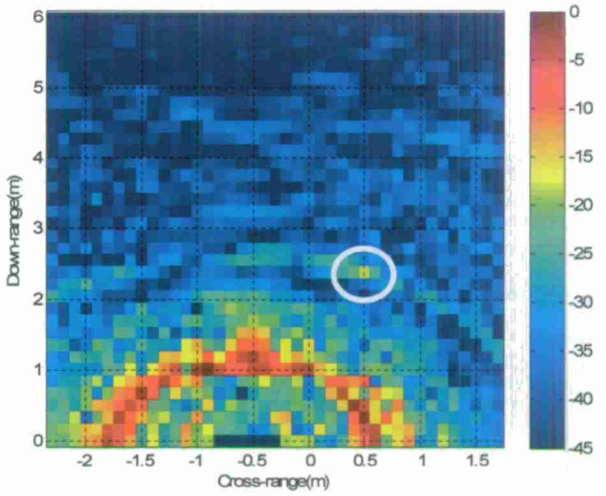


(a)

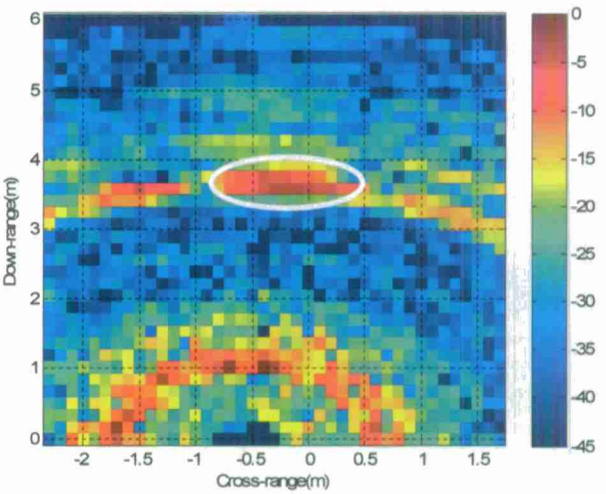


(b)

Fig. 6. Backprojection result without time gating, (a) the stationary target, (b) moving target.

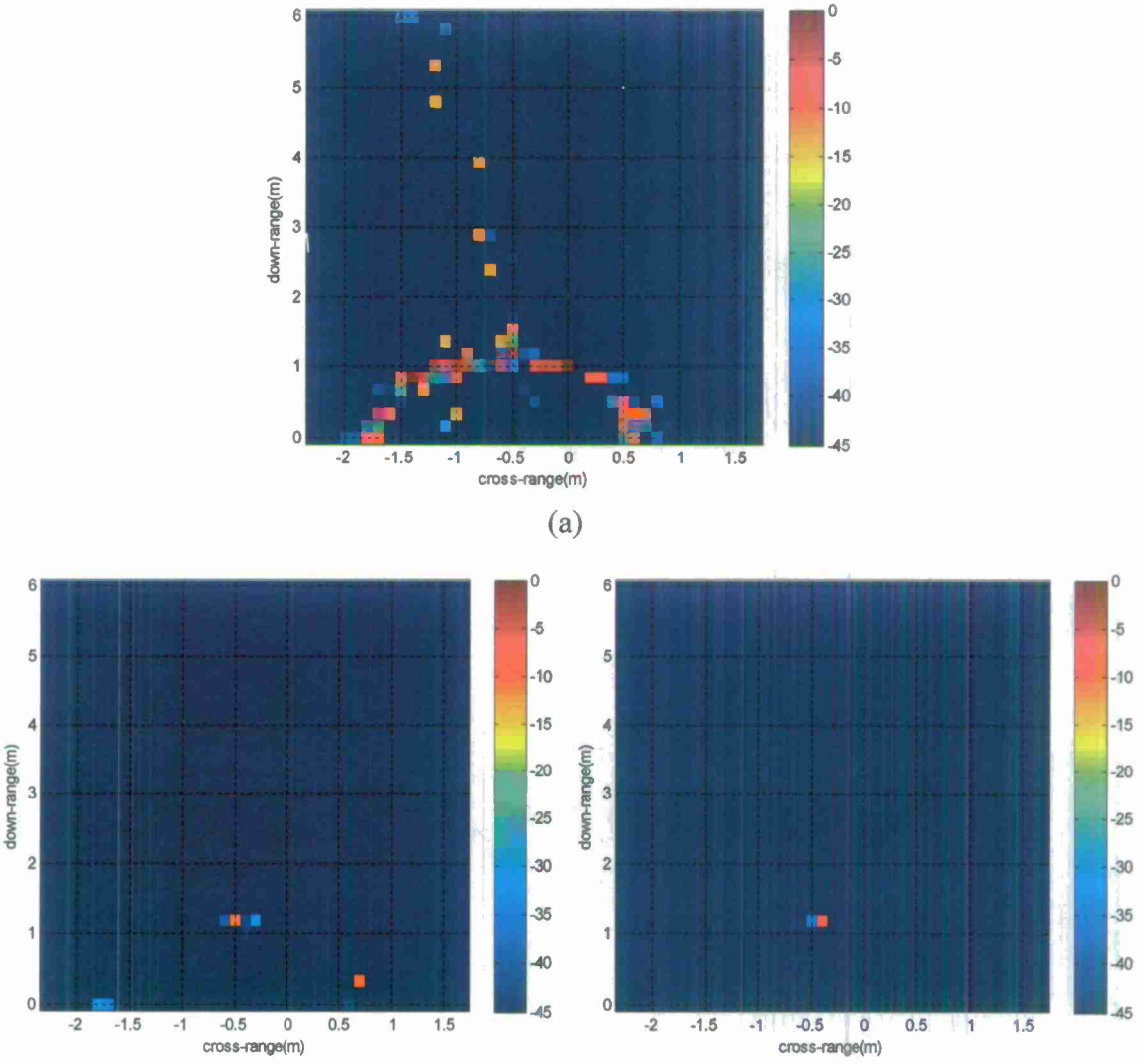


Fig. 7. Imaging result for both stationary and moving targets without time gating, (a) CS reconstructed image $\sigma(0,0)$, (b) CS reconstructed image $\sigma(0,-0.7)$,(c) CS reconstructed image $\sigma(0,-1.4)$.

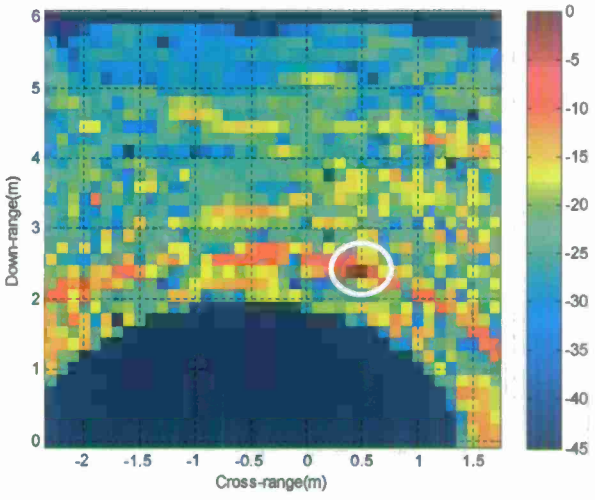


(a)

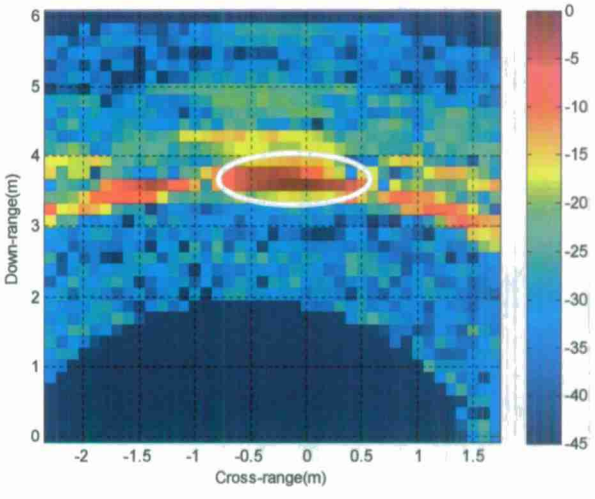


(b)

Fig. 8. Backprojection result after time gating, (a) the stationary target, (b) moving target.

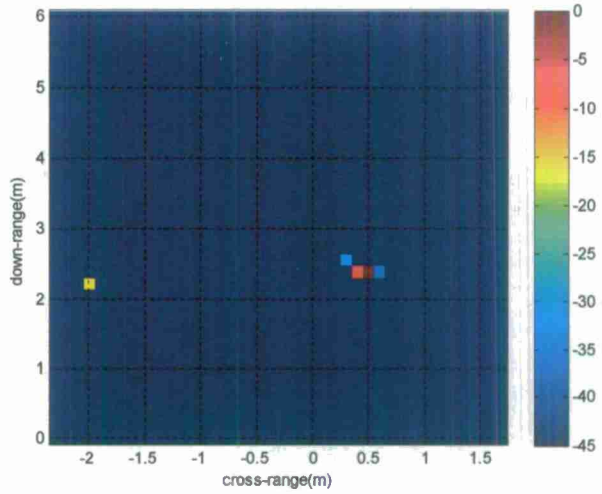


(a)

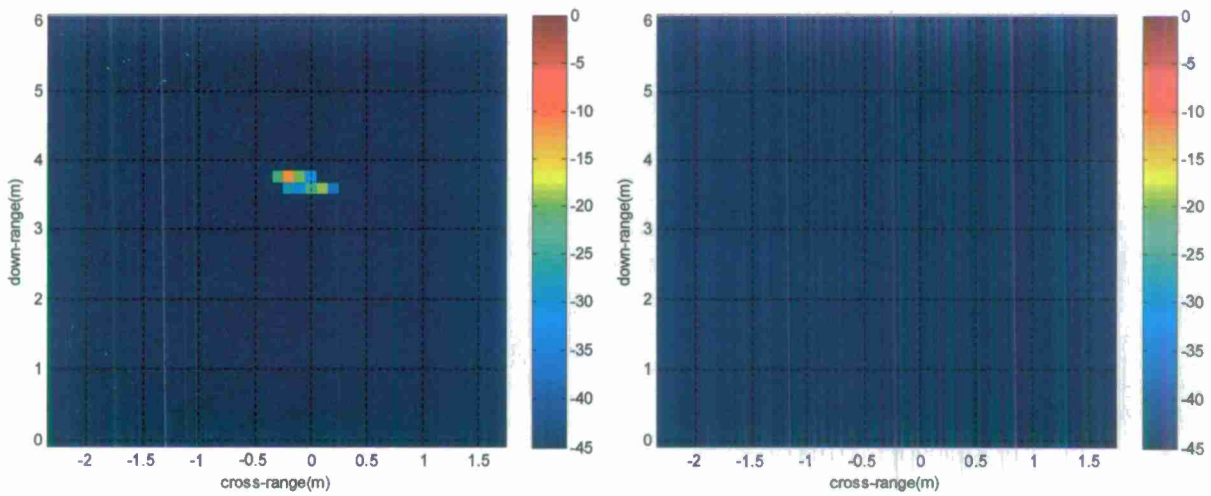


(b) (c)

Fig. 9. Imaging result for both stationary and moving targets after time gating: (a) CS reconstructed image $\sigma(0,0)$, (b) CS reconstructed image $\sigma(0,-0.7)$, (c) CS reconstructed image $\sigma(0,-1.4)$

# Chapter 3

## Partially Sparse Reconstruction of Behind-the-Wall Scenes

### 3.1. Introduction

Detection and localization of targets inside enclosed structures using radio frequency sensors are the primary objectives of urban sensing and through-the-wall radar imaging (TWRI) [1-9]. It is highly desirable to achieve these objectives in an efficient and reliable manner. This goal is primarily challenged due to increasing demands on radar systems to deliver high resolution images in both range and cross-range, which requires use of wideband signals and large array apertures, respectively. In addition, the clutter caused by the wall backscatter can significantly contaminate the radar data and compromise the main intent of providing enhanced system capabilities for imaging of building interiors and tracking of targets behind walls.

Emerging compressive sensing (CS) techniques have recently been used to aid in efficient data acquisition in radar imaging systems for urban sensing applications [10-12]. The capability of CS to reconstruct a sparse signal from far fewer non-adaptive measurements provides a new perspective for data reduction in radar imaging without compromising the imaging quality. Moving target detection and localization inside buildings lends itself readily to the CS paradigm either by removal of stationary background (clutter and stationary targets) via change detection [13] or through exploiting sparsity in the Doppler domain [14]. However, these means are not available when targets of interest are stationary.

In order to detect and localize stationary targets behind walls, wall reflections should be properly suppressed, or significantly mitigated without requiring imaging of a reference or background scene. Several approaches for mitigation of the wall contribution to the received

signal have been proposed in the literature [6, 15-17]. These approaches were originally introduced to work on the full data volume, and were later shown to be equally effective under reduced data volume and within the sparse signal reconstruction framework [18, 19]. More specifically, direct applications of wall clutter mitigation techniques, such as spatial filtering[15] and subspace projection [16, 17], were shown to be effective in [18], provided that the same reduced set of frequencies, or time samples, were used at each antenna position. However, having the same frequency observations or time samples may not always be possible. For instance, some individual frequencies or frequency subbands may be unavailable due to competing wireless services or intentional interferences. For the case when different sets of reduced frequencies are used for different antennas, a scene reconstruction approach was proposed in [19] in which CS was used to reconstruct the individual range profiles, thereby providing the wall clutter mitigation methods with the response measured at the same set of frequencies. However, in addition to an increase in computational complexity, the CS technique in [19] suffers from the following issues: a) Less reduction in data volume compared to the case when the same set of reduced frequencies are used from each antenna, and (b) Loss in reconstruction quality despite the use of a larger amount of data.

In this Chapter, instead of using wall clutter mitigation as a preprocessing step to image formation, we apply the idea of partial sparsity to through-the-wall scene reconstruction under reduced data volume. Partially sparse recovery considers the case when it is known a priori that the scene being imaged consists of two parts, one of which is sparse and the other is expected to be dense [20, 21]. More specifically, we consider the scene reconstruction problem involving a few stationary targets of interest when the building layout is assumed known. This implies that the support of the dense part of the image corresponding to the exterior and interior walls is

assumed known. This knowledge may be available either through building blueprints or from prior surveillance operations. We focus on stepped-frequency synthetic aperture radar (SAR) operation and assume that few frequency observations are available, which could be the same or different from one antenna position to another constituting the set of reduced spatial measurements. Using data collected in a laboratory setting, we demonstrate the effectiveness of the partial sparsity based approach for reconstruction of stationary through-the-wall scenes.

The remainder of this Chapter is organized as follows. Section 3.2 presents the signal model under the assumption of partial sparsity. The fundamental equations for the partially sparse scene reconstruction are provided in Section 3.3. Section 3.4 evaluates the performance of the partially sparse through-the-wall scene reconstruction using real-data collected in a semi-controlled laboratory environment. Conclusions are drawn in Section 3.5.

### 3.2. Partially Sparse Signal Model

Consider the use of a synthetic aperture radar in which a single antenna at one location transmits and receives the radar signal, then moves to the next location, and repeats the same operation along the axis parallel to a homogenous front wall. Assume $N$ antenna locations and a stepped-frequency signal of $M$ frequencies, which are equispaced over the desired bandwidth $\omega_{M-1} - \omega_0$,

$$\omega_m = \omega_0 + m\Delta\omega, \; m = 0,1,\ldots,M-1 \tag{1}$$

where $\omega_0$ is the lowest frequency in the desired frequency band and $\Delta\omega$ is the frequency step size. The scene behind the front wall is assumed to be composed of $P$ point targets and $L$-1 walls, which are parallel to the front wall and to the radar scan direction. It is noted that, as the walls behave as specular reflectors at the operational frequency range for TWRI, no backscattered

signals are received from walls in the scene that are perpendicular to the front wall. We, therefore, exclude perpendicular walls from the signal model.

The component of the received signal corresponding to the $m$th frequency at the $n$th antenna, with phase center at $\mathbf{x}_{tn} = (x_{tn}, 0)$, due to the $P$ point targets is given by [5]

$$y_{tgt}(m,n) = \sum_{p=0}^{P-1} \sigma_p \exp(-j\omega_m \tau_{p,n}) \tag{2}$$

where $\sigma_p$ is the complex reflectivity of the $p$th target and $\tau_{p,n}$ is the two-way traveling time between the $n$th antenna and the $p$th target. On the other hand, the reflections from the $L$ walls measured at the $n$th antenna location corresponding to the $m$th frequency can be expressed as[15]

$$y_{wall}(m,n) = \sum_{l=0}^{L-1} \sigma_{w,l} \exp(-j\omega_m \tau_{w,l}) \tag{3}$$

where $\sigma_{w,l}$ is the complex reflectivity of the $l$th wall and $\tau_{w,l}$ is the two-way traveling time of the signal from the $n$th antenna to the $l$th wall. Note that since the scan direction is parallel to the walls, the delay $\tau_{w,l}$ does not depend on the variable $n$ and is a function only of the downrange distance between the $l$th wall and the antenna baseline. The $n$th received signal corresponding to the $m$th frequency is, thus, given by

$$y(m,n) = y_{tgt}(m,n) + y_{wall}(m,n) \tag{4}$$

Assume that the scene being imaged or the target space is divided into a finite number of grid-points, say $Q$, in crossrange and downrange. Let $\mathbf{y}_n$ represent the received signal vector corresponding to the $M$ frequencies and the $n$th antenna location, and $\mathbf{s}$ be the concatenated $Q \times 1$

scene reflectivity vector corresponding to the spatial sampling grid. Under the assumption that the building layout is known a priori, $\mathbf{s}$ can be expressed as $\mathbf{s} = [\mathbf{s}_1^T \ \mathbf{s}_2^T]^T$, where $\mathbf{s}_1 \in \mathbb{C}^r$ is the dense part whose support is known and $\mathbf{s}_2 \in \mathbb{C}^{Q-r}$ is the sparse part. Then, using eqns. (2)-(4), we obtain the matrix-vector form

$$\mathbf{y}_n = \mathbf{A}_{n1}\mathbf{s}_1 + \mathbf{A}_{n2}\mathbf{s}_2 \tag{5}$$

where $\mathbf{A}_{n2}$ is an $M \times (Q-r)$ dictionary matrix, whose rows are given by

$$[\mathbf{A}_{n2}]_m = [\exp(-j\omega_m \tau_{0,n}) \quad \exp(-j\omega_m \tau_{1,n}) \quad \cdots \quad \exp(-j\omega_m \tau_{(Q-1),n})] \tag{6}$$

with $\tau_{q,n}$ being the two-way traveling time between the $n$th antenna and the $q$th grid-point, and $\mathbf{A}_{n1}$ is an $M \times r$ dictionary matrix, whose rows are given by,

$$[\mathbf{A}_{n1}]_m = [\exp(-j\omega_m 2z_0/c)\Im_{0,n} \quad \exp(-j\omega_m 2z_1/c)\Im_{1,n} \quad \cdots \quad \exp(-j\omega_m 2z_{(Q-1)}/c)\Im_{(Q-1),n}] \tag{7}$$

In (7), $z_q$ represents the downrange coordinate of the $q$th grid-point, and $\Im_{q,n}$ is an indicator function which assumes a unit value only when the $q$th grid-point lies in front of the $n$th antenna, as illustrated in Fig. 1. That is, if $x_q$ represents the crossrange coordinate of the $q$th grid-point and $\delta x$ represents the crossrange sampling step, then $\Im_{q,n} = 1$ provided that $x_q - \delta x/2 \le x_{tn} < x_q + \delta x/2$.

Equation (5) considers the contribution of only one antenna location. Stacking the measurement vectors corresponding to all $N$ antennas to form a tall vector $\mathbf{y}$, we obtain the linear system of equations

$$\mathbf{y} = \mathbf{A}_1\mathbf{s}_1 + \mathbf{A}_2\mathbf{s}_2 \tag{8}$$

where

$$\mathbf{y} = [\mathbf{y}_0^T \quad \mathbf{y}_1^T \quad \cdots \quad \mathbf{y}_{N-1}^T]^T,$$
$$\mathbf{A}_1 = [\mathbf{A}_{01}^T \quad \mathbf{A}_{11}^T \quad \cdots \quad \mathbf{A}_{(N-1)1}^T]^T, \tag{9}$$
$$\mathbf{A}_2 = [\mathbf{A}_{02}^T \quad \mathbf{A}_{12}^T \quad \cdots \quad \mathbf{A}_{(N-1)2}^T]^T$$

Note that the vector $\mathbf{y}$ contains the full dataset corresponding to the $N$ antenna locations and the $M$ frequencies. For the case of reduced data volume, consider $\xi$, which is a $K$ ($<< MN$) dimensional vector consisting of elements randomly chosen from $\mathbf{y}$ as follows,

$$\xi = \mathbf{\Phi y} = \mathbf{\Phi A}_1\mathbf{s}_1 + \mathbf{\Phi A}_2\mathbf{s}_2 \tag{10}$$

where $\mathbf{\Phi}$ is a $K \times MN$ measurement matrix of the form,

$$\mathbf{\Phi} = \text{kron}(\psi, \mathbf{I}_{K_1}) \cdot \text{diag}\{\varphi_0, \varphi_1, \ldots, \varphi_{N-1}\}, \qquad K = K_1 K_2 \tag{11}$$

In (11), 'kron' denotes the Kronecker product, $\mathbf{I}_{K_1}$ is a $K_1 \times K_1$ identity matrix, $\psi$ is a $K_2 \times N$ measurement matrix constructed by randomly selecting $K_2$ rows of an $N \times N$ identity matrix, and $\varphi_n, n = 0, \ldots, N-1$, is a $K_1 \times M$ measurement matrix constructed by randomly selecting $K_1$ rows of an $M \times M$ identity matrix. We note that $\psi$ determines the reduced antenna locations, whereas $\varphi_n$ determines the reduced set of frequencies corresponding to the $n$th antenna location.

### 3.3. Partially Sparse Reconstruction

Given the reduced set of measurements $\xi$, the scene being imaged can be reconstructed under the assumption of partial sparsity by solving the following optimization problem [20, 21]

$$\hat{\mathbf{s}} = \arg\min_{\mathbf{s}} \|\mathbf{s}_2\|_1 \text{ subject to } \xi = \mathbf{\Phi A}_1\mathbf{s}_1 + \mathbf{\Phi A}_2\mathbf{s}_2 \tag{12}$$

The problem in (12) can be solved using convex relaxation algorithms [20]. In this work, we choose an alternate method outlined in [21]. Let $\mathbf{P}$ be the matrix of the orthogonal projection from $\mathbb{C}^Q$ onto $\Re(\mathbf{\Phi A}_1)^\perp$, where $\Re(\mathbf{\Phi A}_1)^\perp$ is the orthogonal complement of the range space of the matrix $\mathbf{\Phi A}_1$. If $\mathbf{\Phi A}_1$ has full rank, then $\mathbf{P}$ can be expressed as

$$\mathbf{P} = \mathbf{I}_K - (\mathbf{\Phi A}_1)((\mathbf{\Phi A}_1)^H(\mathbf{\Phi A}_1))^{-1}(\mathbf{\Phi A}_1)^H \tag{13}$$

where $\mathbf{I}_K$ is a $K \times K$ identity matrix and the superscript '$H$' denotes the Hermitian operation. On the other hand, if $\mathbf{\Phi A}_1$ has a reduced rank, then we have to resort to the singular value decomposition (SVD) of $\mathbf{\Phi A}_1$ to obtain the matrix $\mathbf{P}$. Let the SVD of $\mathbf{\Phi A}_1$ be given by

$$\mathbf{\Phi A}_1 = [\mathbf{U}_{11}\ \mathbf{U}_{12}]\begin{bmatrix}\tilde{\mathbf{\Lambda}} & \mathbf{0} \\ \mathbf{0} & \mathbf{0}\end{bmatrix}\begin{bmatrix}\mathbf{V}_{11}^H \\ \mathbf{V}_{12}^H\end{bmatrix}, \tag{14}$$

where $\tilde{\mathbf{\Lambda}}$ is a diagonal matrix of the non-zero singular values, $\mathbf{U}_{11}$ and $\mathbf{U}_{12}$ are the matrices consisting of the left singular vectors corresponding to the non-zero and zero singular values, respectively, and $\mathbf{V}_{11}$ and $\mathbf{V}_{12}$ consist of the right singular vectors corresponding to the non-zero and zero singular values, respectively. In this case, $\mathbf{P}$ can be obtained as

$$\mathbf{P} = \mathbf{U}_{12}\mathbf{U}_{12}^H \tag{15}$$

Applying the projection matrix $\mathbf{P}$ to the observation vector $\xi$, we obtain

$$\mathbf{P}\xi = \mathbf{P\Phi A}_1\mathbf{s}_1 + \mathbf{P\Phi A}_2\mathbf{s}_2 = \mathbf{P\Phi A}_2\mathbf{s}_2 \tag{16}$$

We can then recover the $(t-r)$-sparse vector $\mathbf{s}_2$ by solving the problem

$$\hat{\mathbf{s}}_2 = \arg\min_{\mathbf{s}_2} \|\mathbf{s}_2\|_1 \text{ subject to } \mathbf{P}\xi \approx \mathbf{P\Phi A}_2\mathbf{s}_2 \tag{17}$$

where $t$ is the sparsity of the scene $\mathbf{s}$. Note that as the measurements are in general noisy, the equality in (16) has been replaced by approximate equality in the constraint in (17). The problem in (17) belongs to the classical setting of CS and, thus, can be solved using convex relaxation, greedy pursuit, or combinatorial algorithms. In this work, we choose CoSaMP as the reconstruction algorithm primarily because of its ability to handle complex arithmetic [22]. Given $\hat{\mathbf{s}}_2$, the following linear matrix equation

$$\mathbf{\Phi A}_1\mathbf{s}_1 = \xi - \mathbf{\Phi A}_2\hat{\mathbf{s}}_2 \tag{18}$$

can be solved to recover the dense part $\mathbf{s}_1$. If $K \leq r$, least squares can be used to obtain the solution $\hat{\mathbf{s}}_1$. Otherwise, a minimum-norm solution can be obtained.

### 3.4. Experimental Results

In this section, we present scene reconstruction results using the partial sparsity technique using experimental data collected in a laboratory environment and compare the performance with that obtained with classical compressive sensing. In all scene reconstruction results provided in this section, we plot the image intensity on a dB scale with the maximum intensity value in each image normalized to 0dB. The true targets in the images are indicated with white ovals.

#### 3.4.1. CS Measurement Strategy and Windowing for Enhanced Sparsity

The CS measurement strategy employed in this section retains all antenna positions and only applies frequency thinning, as shown in Fig. 2. That is, reduced sets of frequencies are chosen randomly for each of the antenna locations constituting the synthetic aperture. In this case, the expression for measurement matrix $\mathbf{\Phi}$ in (11) reduces to,

$$\mathbf{\Phi} = \text{diag}\{\varphi_0, \varphi_1, \ldots, \varphi_{N-1}\}, \quad K = K_1 \tag{19}$$

Further, as the range sidelobes associated with raw stepped-frequency measurements make the scene appear less sparse, a window function is employed to increase the sidelobe decay rate, thereby reducing the error in the subsequent CS reconstruction [23]. In fact, owing to the particular structure of the measurement matrix $\mathbf{\Phi}$ in (19), the window function can be applied to the CS measurement vector $\xi$ *a posteriori* and need not be incorporated into the dictionary matrices. To elaborate on this point, consider the windowed version of (8) given by

$$\mathbf{y}' = \mathbf{W}'\mathbf{A}_1\mathbf{s}_1 + \mathbf{W}'\mathbf{A}_2\mathbf{s}_2, \quad \mathbf{W}' = \text{diag}\{\mathbf{W}, \mathbf{W}, \ldots, \mathbf{W}\}, \quad \mathbf{W} = \text{diag}\{w_0, w_1, \ldots, w_{M-1}\} \tag{20}$$

where $w_0, w_1, \ldots, w_{M-1}$ are the weights corresponding to the window function, and the dimensions of the matrix $\mathbf{W}'$ are $MN \times MN$. The corresponding CS measurement vector takes the form

$$\xi' = \mathbf{\Phi}\mathbf{y}' = \mathbf{\Phi}\mathbf{W}'\mathbf{A}_1\mathbf{s}_1 + \mathbf{\Phi}\mathbf{W}'\mathbf{A}_2\mathbf{s}_2 \tag{21}$$

where the product $\mathbf{\Phi}\mathbf{W}'$ can be expressed as

$$\mathbf{\Phi}\mathbf{W}' = \text{diag}\{\varphi_0, \varphi_1, \ldots, \varphi_{N-1}\} \cdot \mathbf{W}' = \text{diag}\{\varphi_0\mathbf{W}, \varphi_1\mathbf{W}, \ldots, \varphi_{N-1}\mathbf{W}\} \tag{22}$$

Making use of the fact that the matrix $\varphi_n$ contains no more than one non-zero element in each row and each column, the product $\varphi_n\mathbf{W}$ can be rewritten as [23]

$$\varphi_n\mathbf{W} = \widetilde{\mathbf{W}}_n\varphi_n, \qquad \widetilde{\mathbf{W}}_n = \text{diag}\{w_{i_{0n}}, w_{i_{1n}}, \ldots, w_{i_{(K_1-1)n}}\} \tag{23}$$

where $i_{0n}, i_{1n}, \ldots, i_{(K_1-1)n}$ is the set of column indices corresponding to the non-zero entries of the matrix $\varphi_n$. As a result, instead of solving the partial sparsity based CS reconstruction problem using the new measurements $\xi'$, the subsequent reconstruction finds the solution to the augmented problem

$$\hat{\mathbf{s}} = \arg\min_{\mathbf{s}} \|\mathbf{s}_2\|_1 \text{ subject to } \tilde{\mathbf{W}}\boldsymbol{\xi} = \tilde{\mathbf{W}}\boldsymbol{\Phi}\mathbf{A}_1\mathbf{s}_1 + \tilde{\mathbf{W}}\boldsymbol{\Phi}\mathbf{A}_2\mathbf{s}_2 \tag{24}$$

where $\tilde{\mathbf{W}} = \text{diag}\{\tilde{\mathbf{W}}_0, \ldots, \tilde{\mathbf{W}}_{N-1}\}$.

### 3.4.2. Experimental Setup

A through-the-wall SAR system was set up in the Radar Imaging Lab at Villanova University. A horn antenna, model ETS-Lindgren 3164-04, with an operational bandwidth of 0.7 to 6 GHz, was mounted on a scanner to synthesize a 67-element line array along the *x*-axis, parallel to a 0.14m thick solid concrete wall at a standoff distance of 1.24m, as shown in Fig. 3. The inter-element spacing of the array is 0.0187m. The back and the side walls of the room were covered with RF absorbing material. An Agilent network analyzer, model ENA-5071B with an operation frequency range of 300 kHz – 8.5 GHz, was used for signal generation and data collection. A stepped-frequency signal covering the 1-3 GHz frequency band with a step size of 2.75MHz was employed. Thus, at each scan position, the radar collected 728 frequency measurements over the frequency range of interest. A vertical dihedral was used as the target and placed at 0m in crossrange and 3.03m in downrange, as shown in Fig. 3. The size of each face of the dihedral is 0.39m by 0.28m.

### 3.4.3. Scene Reconstruction Results

The region to be imaged was chosen to be 2.4m x 3.9m centered at (0, 1.95)m and divided into 33 x 53 pixels, respectively. Fig. 4(a) shows the image obtained with backprojection using the full dataset and application of the Hanning window. We can clearly see the ringing due to the antenna mismatch, the front and back faces of the wall, and the target. Note that there is a bias in the downrange locations of the back face of the wall and the target in the image. This is because the speed change in the wall material has not been accounted for in backprojection. Although it

provides good quality images when the full data volume is available, backprojection compromises the image quality when a reduced number of data samples is considered, thereby impeding the detection of targets behind the wall in the image domain. This is illustrated in Fig. 4(b), wherein only 20% of the data volume (146 randomly chosen frequencies for each of the 67 antenna locations) was used for backprojection.

Next, we reconstructed the scene using both classical CS and the partial sparsity-based CS with 20% data volume one hundred times. For each trial, a different random measurement matrix was used to generate the reduced set of measurements, which were then weighted with a Hanning window, followed by classical CS and partial sparsity-based scene reconstructions. In this example, the dense part of the scene, extending in downrange from 0 to 1.8m and in crossrange from -0.7 to 0.7m, consists of 825 pixels, while the sparsity of $s_2$ was chosen as 1. Figure 5(a) depicts the classical CS result, while the partial sparsity based reconstruction of the sparse part of the scene is shown in Fig. 5(b), both averaged over one hundred trials. The scene sparsity in CoSaMP was set to 826 for Fig. 5(a) and 1 for Fig. 5(b). The higher the intensity of a grid point in these images, the greater is the number of times that grid point was populated during the 100 reconstruction trials. We observe from Fig. 5(a) that the classical CS scheme was unable to detect the dihedral in any of the 100 trials because of the strong antenna mismatch and wall responses. On the other hand, the partial sparsity based scheme was able to detect and localize the target with a success rate of 100%. The full scene reconstruction using partial sparsity based technique, averaged over 100 trials, is provided in Fig. 5(c). Least squares was used to recover the dense part of the scene.

## 3.5. Conclusion

In this Chapter, we applied the idea of partial sparsity to scene reconstruction associated with through-the-wall radar imaging of stationary targets. Partially sparse recovery deals with the case when it is known a priori that part of the scene being imaged is dense while the rest is sparse. For the underlying problem, the dense part of the scene corresponds to the building layout and the support of the corresponding part of the image is assumed to be known beforehand. This knowledge may be available either through building blueprints or from prior surveillance operations. Using experimental data collected in a laboratory environment, we demonstrated the effectiveness of the partially sparse reconstruction in detecting and locating stationary targets in through-the-wall scenes while achieving a sizable reduction in the data volume.

## 3.6. References


[1] Amin, M., [Through the Wall Radar Imaging], CRC Press, Boca Raton, (2010).

[2] Debes, C., Riedler, J., Zoubir, A.M. and Amin, M.G., "Adaptive target detection with application to through-the-wall radar imaging," IEEE Trans. Signal Process. 58(11), 5572-5583 (2010).

[3] Chang, P. C., Burkholder, R. L., Volakis, J. L., Marhefka, R. J. and Bayram, Y., "High-frequency EM characterization of through-wall building imaging," IEEE Trans. Geosci. Remote Sens. 47(5), 1375–1387 (2009).

[4] Le, C., Dogaru, T., Nguyen, L. and Ressler, M. A., "Ultrawideband (UWB) radar imaging of building interior: measurements and predictions," IEEE Trans. Geosci. Remote Sens. 47(5), 1409-1420 (2009).

[5] Amin, M. G. and Ahmad, F., "Wideband synthetic aperture beamforming for through-the-wall imaging," IEEE Signal Process. Mag. 25(4), 110-113 (2008).

[6] Dehmollaian, M. and Sarabandi, K., "Refocusing Through the Building Walls Using Synthetic Aperture Radar," IEEE Trans. Geosci. Remote Sens. 46(6), 1589–1599 (2008).

[7] Ahmad, F. and Amin, M. G., "High-resolution imaging using Capon beamformers for urban sensing applications," Proc. IEEE Int. Conf. Acoustics, Speech, and Signal Process. II, 985-988 (2007).

[8] Lai, C. P. and Narayanan, R. M., "Through-wall imaging and characterization of human activity using ultrawideband (UWB) random noise radar," Proc. SPIE 5778, 186-195 (2005).

[9] Ahmad, F. and Amin, M. G., "A noncoherent radar system approach for through-the-wall imaging," Proc. SPIE 5778, 196-207 (2005).

[10] Yoon, Y. and Amin, M. G., "Compressed sensing technique for high-resolution radar imaging," Proc. SPIE 6968, 69681A-1-69681A-10 (2008).

[11] Huang, Q., Qu, L., Wu, B. and Fang, G., "UWB through-wall imaging based on compressive sensing," IEEE Trans. Geosci. Remote Sens. 48(3), 1408-1415 (2010).

[12] Leigsnering, M., Debes, C. and Zoubir, A. M., "Compressive sensing in through-the-wall radar imaging," Proc. IEEE Int. Conf. Acoustics, Speech, and Signal Process., 4008-4011 (2011).

[13] Amin, M., Ahmad, F. and Zhang, W., "A compressive sensing approach to moving target indication for urban sensing," Proc. IEEE Radar Conf., 509-512 (2011).

[14] Amin, M. G. and Ahmad, F., "Through-the-wall moving target detection and localization using sparse regularization," Proc. SPIE, (2012).

[15] Yoon, Y. and Amin, M. G., "Spatial filtering for wall-clutter mitigation in through-the-wall radar imaging," IEEE Trans. Geosci. Remote Sens. 47(9), 3192–3208 (2009).

[16] Chandra, A., Gaikwad, D., Singh, D. and Nigam, M., "An approach to remove the clutter and detect the target for ultra-wideband through-wall imaging," J. Geophysics and Engineering 5(4), 412–419 (2008).

[17] Tivive, F., Bouzerdoum, A. and Amin, M., "An SVD-based approach for mitigating wall reflections in through-the-wall radar imaging," Proc. IEEE Int. Radar Conf., 519–524 (2011).

[18] Targarona, E. L., Amin, M., Ahmad, F. and Nájar, M., "Wall mitigation techniques for indoor sensing within the CS framework," Proc. Seventh IEEE workshop on sensor array and multi-channel signal process., (2012).

[19] Targarona, E. L., Amin, M., Ahmad, F. and Nájar, M., "Compressive sensing for through wall radar imaging of stationary scenes using arbitrary data measurements," Proc. 11th Intl. conf. on information science, signal processing, and their applications, (2012).

[20] Vaswani, N. and Lu, W., "Modified-CS: Modifying compressive sensing for problems with partially known support," *IEEE Trans. Signal Process.* 58(9), 4595–4607 (2010).

[21] Bandeira, A.S., Scheinberg, K. and Vicente, L.N., "On partially sparse recovery," preprint 11-13, Dept. of Mathematics, Univ. Coimbra (2011). [Available: http://www.math.princeton.edu/~ajsb/Publications/partial.pdf]

[22] Needell, D. and Tropp, J. A., "CoSaMP: Iterative signal recovery from incomplete and inaccurate samples," *Appl. Comput. Harmon. Anal.* 26(3), 301-321 (2009).

[23] Craven, L., Nagy, O. and Hanlen, L., "Sparsity enhancing window functions for analogue-to-information conversion with compressed sensing," Proc. Australian Communications Theory Workshop, 93- 96 (2010).

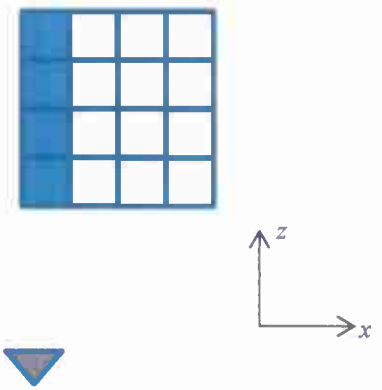


Figure 1. Illustration of the indicator function, which depicts that the indicator function will assume unit values only for the blue pixels when the antenna is at the position shown.

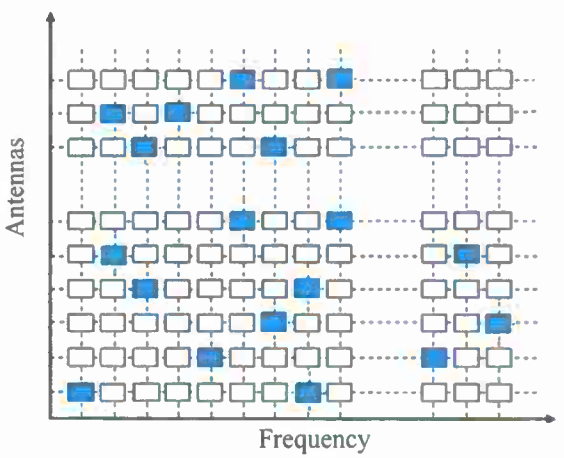


Figure 2. Efficient measurement strategy.

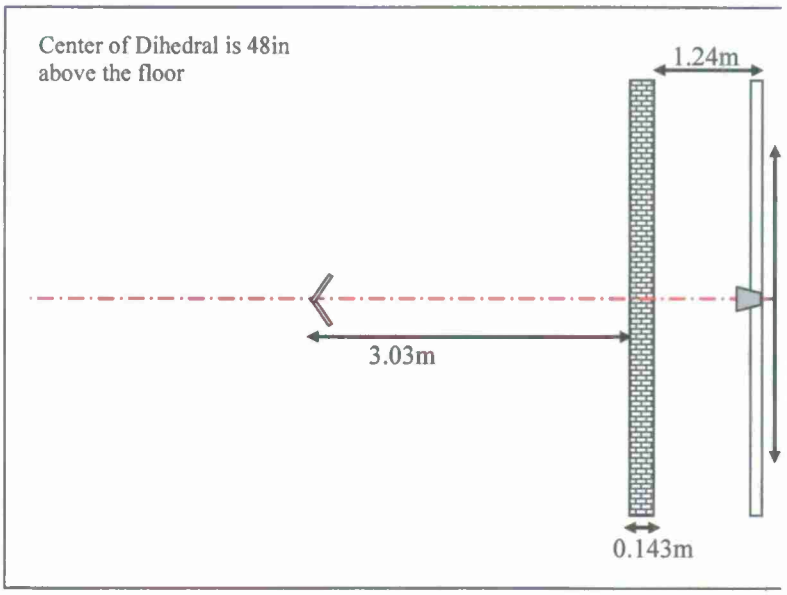


Figure 3. Scene Layout.

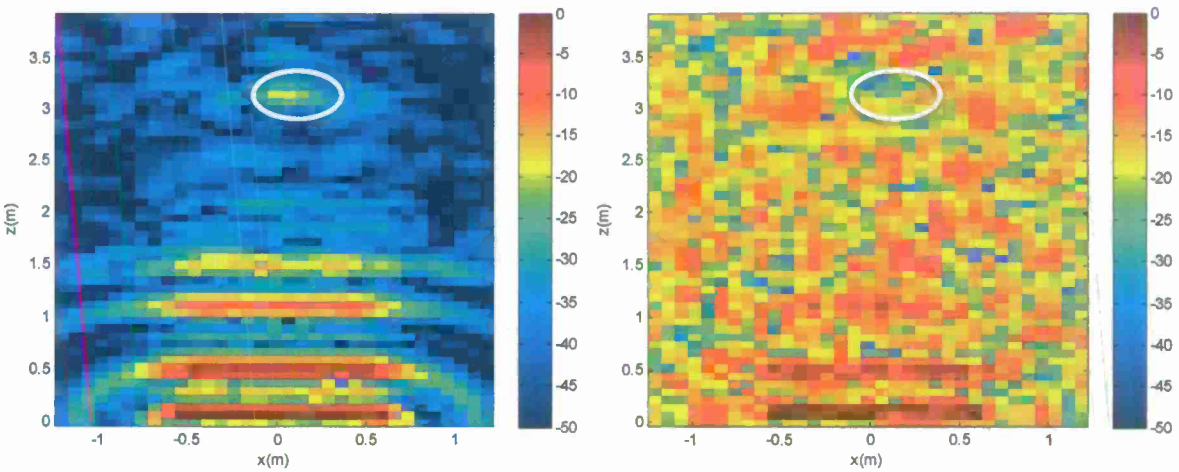


(a) (b)

Figure 4. Backprojected images using Hanning window and (a) Full dataset, and (b) 20% of the data volume.

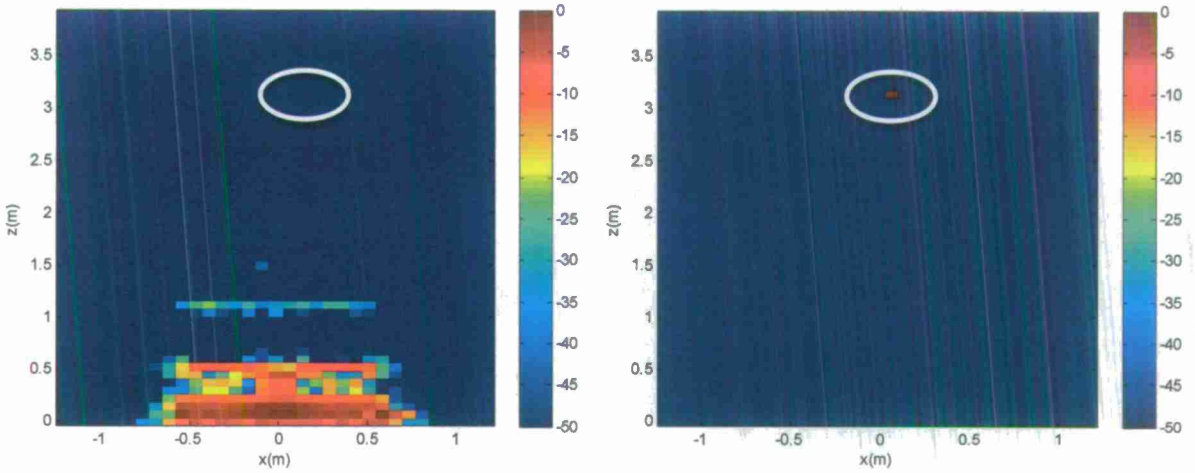


(a) (b)

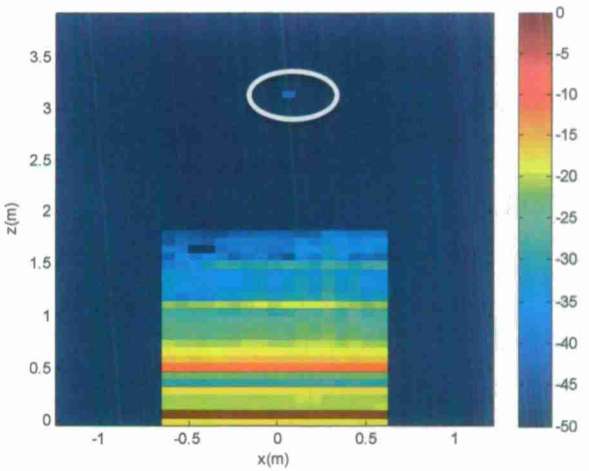


(c)

Figure 5. Scene reconstructions using 20% of the data volume and Hanning window. (a) Classical CS; (b) Partial Sparsity based reconstruction of the sparse part of the scene; (c) Partially sparse reconstruction of the whole scene.

# REPORT DOCUMENTATION PAGE

*Form Approved*
**OMB No. 0704-0188**



| 1. REPORT DATE *(DD-MM-YYYY)* | 2. REPORT TYPE | 3. DATES COVERED *(From - To)* |
|---|---|---|
| 04-23-2013 | Final Technical Report | 05/01/2011 - 09/30/2012 |

**4. TITLE AND SUBTITLE**
Polarimetric and Indoor Imaging Fusion Based on Compressive Sensing

**5a. CONTRACT NUMBER**

**5b. GRANT NUMBER**
N00014-11-1-0576

**5c. PROGRAM ELEMENT NUMBER**

**6. AUTHOR(S)**
Moeness Amin, Fauzia Ahmad, Jiang Qian, and Eva Lagunas

**5d. PROJECT NUMBER**

**5e. TASK NUMBER**

**5f. WORK UNIT NUMBER**

**7. PERFORMING ORGANIZATION NAME(S) AND ADDRESS(ES)**
Center for Advanced Communications, Villanova University
800 E. Lancaster Ave, Villanova, PA 19085

**8. PERFORMING ORGANIZATION REPORT NUMBER**
VU 527906

**9. SPONSORING/MONITORING AGENCY NAME(S) AND ADDRESS(ES)**
Office of Naval Research
875 North Rudolph Street
Arlington, VA 22203-1995

**10. SPONSOR/MONITOR'S ACRONYM(S)**
ONR

**11. SPONSORING/MONITORING AGENCY REPORT NUMBER**

**12. DISTRIBUTION AVAILABILITY STATEMENT**
Approved for Public Release; Distribution is Unlimited.

**13. SUPPLEMENTARY NOTES**

**14. ABSTRACT**
In this report, we apply compressive sensing (CS) techniques to achieve reliable indoor imaging with very few time-frequency-space observations. First, we consider sparsity-driven change detection (CD) for human motion indication. Stationary targets/clutter are removed via CD, resulting in a sparse scene of a few moving humans. We establish appropriate CD models for various possible human motions, which permit scene reconstruction within the CS framework. Second, we consider sparsity-driven joint localization of stationary and moving indoor targets with UWB pulsed radars. We exploit the compact temporal support of UWB signals to suppress the front wall clutter through time gating. The resulting enhancement in the SCR enables application of CS for scene reconstruction. Third, we apply the idea of partial sparsity to indoor scene reconstruction, wherein the scene being imaged is assumed to consist of sparse and dense parts. The support of the dense part corresponding to the exterior and interior walls is known a priori.

**15. SUBJECT TERMS**
Compressive Sensing, Through-the-Wall Radar, Urban Sensing, Indoor Imaging

| 16. SECURITY CLASSIFICATION OF: | | | 17. LIMITATION OF ABSTRACT | 18. NUMBER OF PAGES | 19a. NAME OF RESPONSIBLE PERSON |
|---|---|---|---|---|---|
| a. REPORT | b. ABSTRACT | c. THIS PAGE | UU | 81 | Moeness Amin |
| U | U | U | | | 19b. TELEPONE NUMBER *(Include area code)* 610 519 4263 |